Peripheral Neuronal Activation Shapes the Microbiome and Alters Gut Physiology

Jessica A. Griffiths[1,2+], Bryan B. Yoo[1+], Peter Thuy-Boun[3++], Victor Cantu[4++], Kelly Weldon[5,6,++], Collin Challis[1], Michael J. Sweredoski[1], Ken Y. Chan[1#], Taren M. Thron[1], Gil Sharon[1], Annie Moradian[1%], Gregory Humphrey[3], Qiyun Zhu[3], Justin Shaffer[4], Dennis W. Wolan[3], Pieter C. Dorrestein[4,5,6], Rob Knight[4,6,7,8], Viviana Gradinaru[1,2], and Sarkis K. Mazmanian[1,2*]

[1]Division of Biology & Biological Engineering, California Institute of Technology, Pasadena, California, USA, 91125
[2]Aligning Science Across Parkinson's (ASAP) Collaborative Research Network, Chevy Chase, MD, 20815
[3]Departments of Molecular Medicine and Integrative Structural and Computational Biology, The Scripps Research Institute, 10550 North Torrey Pines Road, La Jolla, CA 92037, USA
[4]Department of Pediatrics, University of California San Diego, San Diego, CA, USA
[5]Collaborative Mass Spectrometry Innovation Center, Skaggs School of Pharmacy and Pharmaceutical Sciences, University of California San Diego, San Diego, CA, USA
[6]UCSD Center for Microbiome Innovation, University of California San Diego, San Diego, CA, USA
[7]Department of Computer Science and Engineering, University of California San Diego, San Diego, CA, USA
[8]Department of Engineering, University of California San Diego, San Diego, CA, USA
[+]These authors contributed equally
[++]These authors contributed equally
[#]Present Address: Stanley Center for Psychiatric Research, Broad Institute, Massachusetts Institute of Technology, Cambridge, MA, 02142, USA
[%] Present Address: Precision Biomarker Labs, Cedars-Sinai, 8700 Beverly Blvd. Davis 2904, Los Angeles, CA 90048

ORCIDs: 0000-0002-5586-1567 (J.A.G.); 0000-0001-5868-348X (V.G.); 0000-0003-2713-1513 (S.K.M.)

SUMMARY

The gastrointestinal (GI) tract is extensively innervated by both intrinsic neurons of the enteric nervous system (ENS) and extrinsic neurons of the central nervous system (CNS) and peripheral ganglia that together regulate gut motility, secretion, and immunity. The GI tract also harbors a diverse microbiome, but interactions between the ENS and the gut microbes remain poorly understood. Herein, we activated gut-associated neurons in mice to determine effects on intestinal microbial communities and their metabolites, as well as on host physiology. We used recombinant adeno-associated viral vectors with enhanced tropism for the gut, and no targeting to the brain, to chemogenetically activate either choline acetyltransferase (ChAT)-expressing or tyrosine hydroxylase (TH)-expressing neurons in the periphery. Targeted activation of discrete neuronal subtypes distinctively altered the metagenome, fecal metabolome, and mouse and microbial proteomes. The resulting datasets provide a rich resource, revealing broad and previously unknown roles for $ChAT^+$ and TH^+ neurons in modulating microbiome structure, and providing evidence for novel ENS functions such as shaping bile acid profiles and regulating fungal colonization of the gut. Further, $ChAT^+$ neuronal activation upregulated transcriptional pathways for muscle cell proliferation, angiogenesis, and muscle development. Physiologically, while mice displayed increased fecal output following activation of gut-associated $ChAT^+$ and TH^+ neurons, only $ChAT^+$ neuronal activation resulted in increased colonic migrating motor complexes and diarrhea-like fluid secretion. These findings suggest that specific subsets of peripherally-activated ENS neurons differentially regulate the gut microbiome and GI physiology in mice.

INTRODUCTION

Diverse cell types in the gastrointestinal (GI) tract coordinate physiology within the gut (Furness, 2006) and throughout the body (Rao and Gershon, 2016). The mammalian gut receives and transmits neuronal signals through ~100,000 extrinsic nerve fibers originating from the sympathetic, parasympathetic, and sensory nervous systems (Grundy and Brookes, 2011). The GI tract is also innervated by an extensive network of over 100 million intrinsic neurons organized into two distinct compartments within the GI tract, namely the myenteric plexus and submucosal plexus (Furness et al., 2014). The neurons of the GI tract, composing the enteric nervous system (ENS), have been implicated in processes including digestion (Schneider et al., 2019), immunity (Gabanyi et al., 2016; Muller et al., 2014), and even complex behaviors (Bravo et al., 2011) in mice. Interactions between neurons of the GI tract and other cell types highlight the diverse roles of the ENS. For example, neuronal pathways in the gut regulate nutrient sensation through intestinal enteroendocrine cells (Kaelberer et al., 2018), modulate the epithelial barrier and mucosal immunity (Jarret et al., 2020; Seillet et al., 2020; Talbot et al., 2020), and dynamically interface with the microbiome (Lai et al., 2019; Matheis et al., 2020). Exposure of the ENS to changing diet, microbiome, and xenobiotics creates inputs distinct from those in the central nervous system (CNS), i.e., the brain and spinal cord.

Choline acetyltransferase (ChAT) and tyrosine hydroxylase (TH) are the rate-limiting enzymes in acetylcholine and catecholamine biosynthesis, respectively, and are key chemical mediators of neurotransmission in the brain and the periphery. Acetylcholine is the primary excitatory neurotransmitter of the gut, and cholinergic neurons represent 60% of the ENS, mediating intestinal propulsion and secretion (Nezami & Srinivasan, 2010; Qu et al., 2008). Several studies have established correlations between neuronal activity, abundance, and specific physiological outcomes (Furness, 2012; Hennig et al., 2015; Niesler et al., 2021). For example, age-associated reduction of $ChAT^+$ neurons in the ENS coincides with constipation and evacuation disorders (Nezami & Srinivasan, 2010; Qu et al., 2008), and clinical studies have shown that anticholinergic drugs cause constipation and cholinergic agonists can cause diarrhea (Lott & Jones, 2023; Monane et al., 1993). In a disease context, cholera toxin induces hypersecretion and sustained activation of submucosal $ChAT^+$ neurons in mice (Fung et al., 2018; Wang et al., 2022). Although less characterized, TH^+ neurons and dopamine signaling pathways have also been shown to affect GI motility (Shan Li et al., 2006), and TH^+ neuronal damage in individuals with Parkinson's disease (PD) correlates with increased constipation (Baumuratov et al., 2016; McQuade et al., 2021).

Though known to be important for motility and secretomotor function, ChAT$^+$ and TH$^+$ neurons have not yet been systematically characterized and interrogated for their roles in GI physiology (Furness, 2012; Mittal et al., 2017). One barrier to modulation of neuronal populations in the ENS is its size: 35-40 cm in mice. To circumvent the need for direct delivery of effectors, we leveraged a systemically-delivered engineered adeno-associated virus (AAV) with enhanced tropism for the ENS and other peripheral ganglia of mice (Chan et al., 2017). Importantly, this vector, AAV-PHP.S, does not transduce the CNS, allowing us to uncouple peripheral activation from brain-to-gut signaling. We find that activating gut-associated ChAT$^+$ and TH$^+$ neurons of mice with chemogenetic modulators (Wess et al., 2013) alters the transcriptional and proteomic landscape of the intestines, as well as the gut metagenome and metabolome. Multi-'omic' analyses allow us to characterize detailed and complex host-microbial interactions, and enable prediction of neuronal influences on a number of biological processes in the gut, including providing novel insights into secondary bile acid production and control of fungal populations, among other interesting associations. In addition, we show that activation of gut-associated neurons strikingly impacts GI function, including motility and fluid secretion. Together, this work reveals differential effects of non-brain activation of ChAT$^+$ and TH$^+$ neurons in shaping the gut environment and GI physiology and generates rich datasets as a resource for further exploration (https://github.com/mazmanianlab/Griffiths_Yoo_et_al/).

RESULTS

Distinct spatial localization of ChAT$^+$ and TH$^+$ neurons in the ENS

Broad ENS morphology has been previously characterized using immunohistochemistry (IHC) (Furness, 2006; Qu et al., 2008; Hamnett et al., 2022). To map neurons in mice with higher resolution, we used recombinant AAVs to fluorescently label enteric neurons *in vivo*, and tissue clearing techniques to enhance visualization of intact GI tissue (Hama et al., 2015; Treweek et al., 2015; Yang et al., 2014). Imaging whole tissue, without the need for sectioning, preserves neuronal architectures over large distances and across both longitudinal and cross-sectional axes. The AAV capsid variant AAV-PHP.S is optimized for systemic delivery in mice (Deverman et al., 2016) and displays increased tropism for the peripheral nervous system (PNS), including the ENS (Chan et al., 2017). To further optimize ENS expression, we replaced the CAG promoter used in (Chan et al., 2017) with the human Synapsin 1 (hSYN1) promoter, which has been shown to restrict gene expression to neurons (Chan et al., 2017) and minimize expression in peripheral targets such as the dorsal root ganglia (DRGs) (Haenraets et al., 2017). To assess

off-target effects, we compared expression of AAV-PHP.S-delivered hSYN1-mNeonGreen to that of CAG-mNeonGreen in various non-ENS tissues known to affect GI function (Figure S1). Expression from the hSYN1 construct only sparsely labeled the DRGs and jugular-nodose ganglia, and did not label neuronal projections in the vagus nerve or dorsal root, unlike the previously-used CAG construct (Figures S2A and S2B) (Chan et al., 2017). In the CNS, AAV-PHP.S-hSYN1 did not label neurons in the brain, brainstem, or spinal cord (Figure S3).

We packaged genes encoding fluorescent proteins (tdTomato or mNeonGreen) under control of the hSYN1 promoter into AAV-PHP.S, delivered them systemically, and found that 90% (±2.6% SD) of ENS cells labelled with antibodies against *P*rotein *G*ene *P*roduct 9.5 (PGP9.5), a pan-neuronal protein, co-localized with virally-labelled neurons in the small intestine (SI) and colon (Figure 1A). A single systemic injection of AAV-PHP.S-hSYN1-mNeonGreen at a dose of 10^{12} viral genomes (vg) was sufficient to label spatially diverse regions of the ENS, such as ganglia proximal and distal to the mesentery (Figure S4A). Viral transduction was uniform throughout the SI and colon, aside from a small (~1.5 cm) section of the medial colon that, for unknown reasons, was consistently not well transduced and was therefore excluded from further analysis (Figure S4B).

To explore the general architecture of the ENS, we transduced wild-type mice with a single i.v. injection of a pool of AAV-PHP.S packaging multiple fluorescent proteins (AAV-PHP.S-hSYN1-XFP), which broadly labelled enteric neurons in the gut and enabled us to distinguish cells by distinct colors resulting from stochastic transduction with different combinations of XFPs (Figure 1B). We quantified the number of neurons and ganglia, as well as the ganglion size (i.e., the number of neurons in each ganglion) in the myenteric and submucosal plexuses of seven regions of the SI and two regions of the colon (Figures S5A-S5F). Regions were approximately 1 cm in length and the tissue was sampled every 2-3 cm. We saw that in the SI, the numbers of neurons and ganglia generally increased toward the distal portion of the myenteric plexus, while the converse was true for the submucosal plexus (i.e., lower numbers in distal than proximal regions) (Figures S5A and S5B). Additionally, the size of the ganglia (i.e., the number of neurons per ganglion) increased in the distal region of the SI myenteric plexus, a feature not observed in the submucosal plexus (Figure S5C). While neuronal numbers were similar in the proximal and distal regions of the colonic plexuses (Figure S5D), the number of myenteric ganglia increased (Figure S5E) while the size of each ganglion decreased in the distal colon

(Figure S5F). Interestingly, submucosal neurons in the proximal colon localized to natural folds in the tissue (Figure 1B, dashed lines in lower second-from-right panel).

To visualize ChAT$^+$ and TH$^+$ neurons, we employed mouse lines in which Cre recombinase (Cre) is expressed under the control of the respective gene promoter and engineered viral constructs with the transgene in a double-floxed inverted orientation (DIO) so that the transgene is flipped and expressed in a Cre-dependent manner. After transducing ChAT-Cre or TH-Cre mice with AAV-PHP.S-hSYN1-DIO-XFP, we observed that both neuronal populations occupy spatially distinct layers of the GI tract, with ChAT$^+$ neurons primarily located in the myenteric plexus and TH$^+$ neurons more abundant in the submucosal plexus (Figure 1C). Quantifying this effect, we found more ChAT$^+$ than TH$^+$ neurons in all assayed regions of the myenteric plexus (Figure 1D), although the density of TH$^+$ myenteric neurons increased distally (Figure 1D, 10-fold increase from SI-1 vs SI-7; 2-fold increase from SI-7 vs SI-10/13/15). In the small intestine, by contrast, there were more TH$^+$ than ChAT$^+$ submucosal neurons (Figure 1E). In addition to providing these insights into ENS architecture, this approach for whole tissue imaging without the need for antibody labeling (which has limited penetration to deeper layers) should be broadly useful for profiling other neuronal and non-neuronal cell types in the gut.

Activation of gut-associated neurons reshapes the gut microbiome

The unique spatial organization of ChAT$^+$ and TH$^+$ neurons we observed suggests potentially distinct functions, which we decided to investigate through specific activation of each neuronal population. First, we examined the specificity of AAV-PHP.S-hSYN1 by staining gut-extrinsic PNS ganglia for TH, and found no transduction of TH$^+$ cells in the DRGs or jugular-nodose ganglia (Figures S2B and S2C). ChAT$^+$ neurons are absent in these peripheral ganglia (Figure S2C) (Jakob et al., 2021; Tavares-Ferreira et al., 2022). Prior research has shown that AAV-PHP.S-hSYN1 transduces the prevertebral sympathetic ganglia, which are known to innervate the gut (Challis et al., 2019), but these ganglia also lack ChAT$^+$ neurons (Kaestner et al., 2019). In fact, the vast majority of neurons in the prevertebral sympathetic ganglia are TH$^+$ (Browning & Travagli, 2014; Kaestner et al., 2019).Therefore, for the remainder of the manuscript, we will use the term “gut-associated” to refer to ChAT$^+$ neurons in the ENS, or TH$^+$ neurons in the ENS plus innervating prevertebral sympathetic ganglia.

For cell-specific neuronal activation, we employed a Cre-dependent genetic construct encoding an activating ‘*D*esigner *R*eceptor *E*xclusively *A*ctivated by *D*esigner *D*rugs’ (DREADD), named

hM3Dq, which is a modified neurotransmitter receptor designed to induce neuronal activation when exposed to Compound 21 (C21), a “designer drug” specific to this receptor (Thompson et al., 2018). We validated functional gene delivery and expression using intestinal explants from a ChAT-Cre mouse transduced with the activating DREADD and a construct encoding the calcium sensor GCaMP6f, observing a gradual increase in fluorescence consistent with a calcium transient following administration of C21 (Figure S5G and Video Supplement 1).

We reasoned that neuronal activation in the gut may impact the composition and community structure of the gut microbiome. Accordingly, we transduced ChAT-Cre or TH-Cre mice with either virus carrying the activating DREADD (AAV-PHP.S-hSYN1-DIO-hM3Dq-mRuby2) or a control virus expressing only the fluorescent reporter protein (AAV-PHP.S-hSYN1-DIO-mRuby2). We performed shotgun metagenomics on a longitudinal series of fecal samples collected prior to and following ChAT$^+$ or TH$^+$ neuron activation by C21 (on days 2, 6, and 10 of C21 administration), as well as contents of the terminal cecum collected on day 10 (Figure 2A). In ChAT$^+$-activated mice, Faith’s phylogenetic diversity (i.e., alpha-diversity) decreased dramatically in the day 10 fecal and cecal samples (Figure 2B), with many microbial taxa less abundant (Figures 2I-2K; Figure S6; Figure S7). In contrast, TH$^+$-activated mice displayed similar phylogenetic diversity to controls throughout the experiment (Figure 2B). Using weighted UniFrac distances and principal coordinate analysis (PCoA) to determine the composition of microbial communities (i.e., beta-diversity), we observed a distinction between ChAT$^+$-activated and control animals in both feces and cecal contents, a shift that was absent in samples from TH$^+$-activated mice and controls (Figures 2C-H). Over the experimental time course, Verrucomicrobia became significantly enriched in ChAT$^+$-activated mice (Figure 2I). To explore differentially abundant bacterial taxa, we used linear discriminant analysis effect size (LEfSe) (Segata et al., 2011) and generated cladograms depicting the phylogenetic relationships of differentially abundant taxa (Figures 2J-2M). This analysis revealed that the bacterial species *Akkermansia muciniphila* drove the increase in Verrucomicrobia we observed in ChAT$^+$-activated mice (Figures 2N and 2O).

In addition to identifying microbial species, metagenomic analysis can reveal gene families and pathways that are differentially abundant in the microbiome. ChAT$^+$-activated mice, but not TH$^+$-activated mice, showed changes in beta-diversity of both gene families and pathways, with shifts evident in the cecal contents and feces collected 9 days after activation (Figures 2P-2S). The most distinguishing features were highly represented in the control group and

downregulated in ChAT$^+$-activated mice and were mainly associated with bacterial processes, such as nucleotide biosynthesis and metabolism, and protein translation and transport (Figures 2P-2S; Figures S7C and S7D). This downregulation is consistent with the decrease in bacterial alpha-diversity we observed in ChAT$^+$-activated mice (Figure 2B). We conclude that neuronal activation actively reshapes the gut microbiome at community, species, and genetic levels, with considerable differences between the effects of ChAT$^+$ and TH$^+$ neurons.

Neuronal stimulation impacts the gut metabolome

Given the intimate and intertwined mouse and microbial co-metabolism, the changes in the microbial metagenome we observed in response to neuronal activation led us to predict that there would also be alterations in the profile of gut metabolites. We therefore performed untargeted metabolomics using liquid chromatography with tandem mass spectrometry (LC-MS/MS) to assay molecular changes in cecal contents and feces following neuronal activation in the gut. In both ChAT$^+$- and TH$^+$-activated neurons, compared to nonactivated controls (no DREADD), we observed a strong separation of metabolome profiles in cecal samples taken one hour following the last C21 injection (Figures 3A and 3B). Thus, targeted activation of ChAT$^+$ and TH$^+$ gut associated neurons appears to strongly influence the gut metabolome.

To contextualize these data, we applied the Global Natural Products Social Molecular Networking (GNPS) tool (Wang et al., 2016), an open-access mass spectrometry repository and analysis pipeline. GNPS revealed metabolic networks of both annotated and unannotated molecules in the cecal contents of ChAT$^+$-activated and TH$^+$-activated mice (Figures 3C and 3D), allowing us to identify metabolites with differential abundance between control and activated samples. Activation of TH$^+$ neurons strongly increased metabolites whose closest spectral matches were linoelaidic acid (ID: 626), oleanolic acid methyl ester (ID: 378), and coproporphyrin I (ID: 739). Metabolites that spectrally resembled xanthine (ID: 259), genistein (ID: 846), and trans-ferulic acid (ID: 707) were decreased upon activation of TH$^+$ neurons (Table S1).

In both ChAT$^+$-activated and TH$^+$-activated mice, the molecular networks largely consisted of level 3 annotations (based on the Metabolomics Standards Initiative (MSI) (Sumner et al., 2007)) of compounds belonging to the bile acid molecular family and their conjugates, as well as unannotated analogs (Figures 3C-3D). Primary bile acids are chemicals derived from host (mouse) cholesterol biosynthesis, which are subsequently co-metabolized by gut bacteria into

secondary bile acids (Aries et al., 1969; Sakai et al., 1980). Interestingly, metabolites with a closest spectral match to the primary bile acid cholic acid (IDs: 108, 114, 215, 219, 221, 224, 259) were significantly enriched in the cecum of ChAT$^+$-activated mice (Figures 3D-3F; Table S1). Additional metabolites that spectrally resemble tauro-conjugated primary bile acids, such as taurocholic acid (IDs: 234, 248) and taurohyocholic acid (ID: 235), trended upwards. Conversely, features matching the spectra of secondary bile acids and bile acid metabolites such as ursodeoxycholic acid (ID: 13), deoxycholic acid (ID: 100), beta-hyodeoxycholic acid (IDs: 1, 143) and 12-ketodeoxycholic acid (IDs: 19, 138) were decreased in ChAT$^+$-activated mice (Figures 3D-3F). These data suggest that activation of ChAT$^+$ neurons may modulate, either directly or indirectly, primary bile acid secretion and/or metabolism to secondary bile acids, which have been implicated in a number of metabolic and immunologic functions, as discussed below.

Neuronal subpopulations differentially shape the gut luminal proteome

Proteins from the mouse, gut microbes, and diet converge and interact in the GI tract (Albenberg and Wu, 2014). We performed untargeted label-free proteomics by LC-MS/MS of cell-free supernatants of the cecal contents from ChAT$^+$-activated and TH$^+$-activated mice and controls collected one hour following the final C21 treatment (see Figure 2A). Consistent with the increase in cecal bile acid metabolites that we observed in ChAT$^+$-activated mice, we report an increased abundance of Niemann-Pick C1-Like 1 protein (NPC1L1) in the cecum of these mice (Figure 4A). NPC1L1 is expressed on the apical surface of enterocytes, and is integral to the absorption of free cholesterol, the precursor of bile acids, from the lumen (Jia et al., 2011). Goblet cell-related proteins, specifically Mucin-19 (MUC19) and Zymogen granule 16 (ZG16), a protein localized to secretory granules (Rodríguez-Piñeiro et al., 2013), also trended upwards following ChAT$^+$ neuronal activation (Figure 4A). Conversely, one of the most highly downregulated proteins was an aldehyde dehydrogenase (Q3U367) encoded by the *Aldh9a1* gene, which is involved in the catalytic conversion of putrescine to gamma-aminobutyric acid (GABA) (Matsushima et al., 1986). While GABA is the primary inhibitory neurotransmitter in the CNS, little is known about its role in the ENS. The most significantly upregulated proteins in cecal contents of ChAT$^+$-activated mice were pancreatic digestive enzymes including chymopasin (CTRL), chymotrypsinogen B1 (CTRB1), and pancreatic lipase related protein 2 (PNLIPRP2) (Figure 4A). Accordingly, network analysis of upregulated proteins revealed that KEGG pathways associated with digestion represent the majority of the network (Figure 4B). This is consistent with evidence that cholinergic, viscerofugal neurons send signals from the GI

tract to other organs of the digestive system, including the pancreas (Furness et al., 2014). Cholinergic innervation of the pancreas plays a significant role in regulating pancreatic functions, such as the secretion of digestive enzymes and insulin release (Li et al., 2019).

Peripheral activation of TH^+ gut-associated neurons also altered the luminal proteome of the cecum. Notably, 88% (52/59) of the differentially abundant proteins ($p_{adj.}<0.25$) were distinct from those identified in $ChAT^+$-activated mice. The overall direction of the effect was also reversed: ~90% of differentially-abundant cecal proteins in TH^+-activated mice were upregulated (53/59), compared to ~18% in $ChAT^+$-activated mice (20/112), suggesting that activation of distinct neuronal subsets is associated with opposing changes in GI function. We observed signatures of increased protein-protein interactions in cecal contents of TH^+-activated mice, evidenced by more network nodes and connections (Figure 4D). Filamin B (FLNB) and spectrin beta chain, non-erythrocytic 1 (SPTBN1) were two of the most significantly enriched proteins following TH^+ neuron activation (Figure 4C). Both are associated with the intestinal brush border and membrane vesicles (Donowitz et al., 2007; McConnell et al., 2011). Accordingly, coatomer proteins also trended upward (COPA and COPB2) (Figure 4C) and vesicle-mediated transport was one of the major protein networks altered (Figure 4D). Other upregulated protein interaction networks were associated with metabolic pathways, ribosomal activity, and the immune system (Figure 4D). For example, the immune-related proteins immunoglobulin heavy constant alpha (IGHA) (in $ChAT^+$-activated), immunoglobulin heavy constant gamma 2C (IGHG2C), and complement component 3 (in TH^+-activated) trended upward (Figures 4A and 4C).

Perhaps the most intriguing observation was the strong depletion of acidic mammalian chitinase (CHIA) upon activation of TH^+ neurons (Figure 4C). Chitin is a natural polysaccharide that is a major component of fungal cell walls (Latgé, 2007), but intestinal chitinases are poorly studied in mice. This result prompted us to query the pan-proteomic dataset against a microbial protein database, which revealed that the decrease in CHIA abundance following TH^+ neuron activation was accompanied by a large bloom in fungal-associated peptides in the microbiome (~59% of peptides mapped to any microbe) (Figure 4E). In contrast, fungal peptides represented only ~0.4% of enriched peptides in the lumen of $ChAT^+$-activated mice (Figure 4F). Unfortunately, we were unable to corroborate these proteomic data with metagenomics since the DNA extraction method we used was not optimized for fungi. However, these findings suggest that the reduced chitinase production of activated TH^+ cells is directly associated with a dramatic increase in

fungal proteins, which, if experimentally validated in future, would represent a novel circuit by which the gut-associated neurons of mice regulates fungal load in the gut.

Activation of ChAT$^+$ and TH$^+$ neurons alters the intestinal transcriptome

Given the changes to the gut microbiome, proteome and metabolome that we observed, we were interested in the tissue-level impact of neuronal activation on the intestinal transcriptome. We therefore profiled gene expression with QuantSeq, a quantitative 3' mRNA-sequencing technology, in 1 cm of tissue from the distal SI and proximal colon harvested one hour after the last C21 injection. Rapid and transient expression of immediate early genes (IEGs) is widely used as a measure of increased neuronal activity (Wu et al., 2017), and the IEGs *Fos*, *Egr1*, *Jun*, and *Klf2* were among the most significantly upregulated transcripts we identified in the SI and colon of both ChAT$^+$- and TH$^+$-activated mice (Figures 5A-5D) . These IEGs are also known to be upregulated during growth and differentiation of highly active cell types such as immune cells (Bahrami and Drabløs, 2016; Ramirez-Carrozzi et al., 2009), smooth muscle cells (Miano et al., 1993), and intestinal epithelial cells (Flandez et al., 2008).

In the distal SI, we found similar numbers of differentially-expressed genes (DEGs; $p_{adj.}<0.05$) in ChAT$^+$-activated mice (162 DEGs) and TH$^+$-activated mice (165 DEGs) (Figures 5A and 5C). The direction of regulation differed, however, with ~73% of DEGs upregulated upon ChAT$^+$ activation (118 up, 44 down) and ~58% of DEGs downregulated upon TH$^+$ activation (69 up, 96 down). IEGs followed this overall pattern, with 29 upregulated in the distal SI of ChAT$^+$-activated mice but only two upregulated in TH$^+$-activated mice (Figure 5E), and three (i.e., *Hbegf, Soca3, Mcl1*) downregulated (Figure 5C). Similar proportions of DEGs were upregulated in the proximal colon of both ChAT$^+$-activated (169 up, 84 down) and TH$^+$-activated mice (130 up, 62 down) (Figures 5B and 5D). Given the enrichment in fungal proteins and reduction in the level of the CHIA protein in the TH$^+$-activated mice, we explored potential immune responses to fungi but found no obvious inflammatory signals compared to control mice (Table S3).

To gain insight into the cellular functions of DEGs, we used Gene Set Enrichment Analysis (GSEA) (Figures 5F-I; Table S2). Notably, the most highly enriched gene ontology (GO) term for the distal SI of ChAT$^+$-activated mice was “regulation of smooth muscle cell proliferation” (Figure 5F), whereas in TH$^+$-activated mice it was “response to bacteria” (Figure 5H), consistent with the increase in immune-related responses suggested by our proteomic dataset. In the proximal colon, we observed similar GO pathways in ChAT$^+$-activated and TH$^+$-activated mice (Figures

5G and 5I), suggesting that transcriptomic signatures may depend on the context of the activated neurons. In the SI, ChAT$^+$ neurons predominantly border muscle cells in the myenteric plexus, while TH$^+$ neurons neighbor epithelial and immune cells which respond to bacteria in the submucosal plexus of the distal SI (see Figures 1C-1E). In the colon, both neuronal subsets are abundant in the myenteric plexus (see Figure 1D). In both myenteric and submucosal plexuses, we saw a wider breadth of pathways upregulated by activation of ChAT$^+$ neurons than TH$^+$ neurons, with ChAT$^+$ neuronal activation impacting diverse cellular functions in the GI tract, involving endothelial, epithelial, immune, and adipose cells (Figure 5G; Table S2).

Differential functional GI outcomes of activation of ChAT$^+$ and TH$^+$ neurons

Motivated by the complexity of responses we observed following activation of neuronal populations in the gut, we decided to assay functional GI outcomes. Both ChAT$^+$ and TH$^+$ neuronal populations are known to be important for motility and secretory function (Furness, 2012; Mittal et al., 2017), but they have never been specifically modulated to study GI physiology in a freely behaving mammal. Activation of either ChAT$^+$ or TH$^+$ gut-associated neurons resulted in faster whole gut transit time, increased fecal pellet output, and mass of cecal contents compared to control mice (Figures 6A-C). Fecal pellets from ChAT$^+$-activated, but not TH$^+$-activated, mice had increased water content, which is consistent with reports in the literature of involvement of ChAT$^+$ enteric neurons in fluid secretion (Figures 6D-6F) (Fung et al., 2018; Monane et al., 1993; Nezami & Srinivasan, 2010). This distinction is particularly notable given the higher concentration of TH$^+$ neurons than ChAT$^+$ neurons in most regions of the submucosal plexus (see Figure 1), which is largely responsible for fluid secretion and absorption (Furness, 2006). Daily administration of C21 for 9 days to control mice (no DREADD) did not cause any obvious health impairment and the mice maintained body weight throughout the experimental period (Figures S6C and S6D). TH$^+$-activated mice also maintained body weight, but ChAT$^+$-activated animals experienced slight weight loss that likely reflects the diarrhea-like phenotype over 9 consecutive days. To further examine gut motility in the absence of extrinsic innervation, we analyzed propulsive colonic migrating motor complexes (CMMCs) in an *ex vivo* system. Activation of ChAT$^+$ neurons by C21 administration resulted in more frequent migration of motor complexes (Figures 6G, 6I, and 6J; Table S4), whereas activation of TH$^+$ neurons had no effect on CMMCs (Figure 6H; Table S4). The discrepancy between the *in vivo* and *ex vivo* results we observed may be due to activation of TH$^+$ neurons in the sympathetic prevertebral ganglia that project to the gut (Furness, 2006). Overall, these data reveal that

ChAT$^+$, but not TH$^+$, neurons in the gut mediate intestinal fluid balance and *ex vivo* colonic motility.

DISCUSSION

While early pioneers of neuroscience in the 20th century focused on the ENS as a model, more recent research has centered on the brain, and our understanding of the CNS has outpaced that of other neuronal systems in the body. As a result, basic knowledge of many aspects of neuronal architecture and function within the gut remain rudimentary (Fung et al., 2018; Monane et al., 1993; Nezami & Srinivasan, 2010). Here, using a viral delivery system with enhanced tropism for the ENS, we mapped the distribution of ChAT$^+$ and TH$^+$ neurons across the mouse GI tract and assayed the complex effects of their peripheral activation on physiology and function. Although the DREADD-based activation paradigm we use in this study is inherently artificial, the results reveal strikingly different roles for neuronal populations, with nearly every feature characterized (spatial distribution, metagenomic, metabolic, transcriptional, and proteomic profiles, and even physiological output) unique to cell type.

The viral vector we used, AAV-PHP.S, can transduce other neuronal subtypes in the PNS such as those in the DRGs and, with a strong ubiquitous promoter, induce transgene expression (Chan et al., 2017). To limit this off-target effect, we utilized a weaker promoter with increased ENS specificity and focused our analyses on GI tissue and lumen. By thus excluding most known extrinsic innervation pathways, we uncover cell-type-specific effects of gut-associated neuronal activation that are independent of signaling from the brain. It was recently shown that a similar strategy using AAV-PHP.S-hSYN1 in ChAT-Cre mice also labels ChAT$^+$ neurons in cardiac ganglia, and activation of cholinergic neurons reduces heart rate and blood pressure (Rajendran et al., 2019; Roy et al., 2015). Cardiac afferent neurons signal through the vagus nerve and jugular-nodose ganglia to the brain, and in sensory pathways through the DRGs and spinal cord (Mohanta et al., 2023). Though there is no known direct route for signaling from cardiac ganglia to gut-associated neurons, it is possible that the gut may be impacted by an indirect route involving the CNS. In the future, further refinement of AAVs through directed evolution may generate serotypes with exclusive tropism for the ENS and allow full separation of the functions of intrinsic and extrinsic activation of gut-associated neuronal subsets. Since the hSYN1 promoter we used has been shown to drive expression only in neurons (Finneran et al., 2021; Kügler et al., 2003), we did not characterize other cell types, such as enteroendocrine cells (EECs), also called neuropod cells, which were recently shown to form synapses with

enteric neurons and contribute to sensory transmission from the gut to the brain through the vagus nerve. Since these cells turn over every few days (Moran et al., 2008) and have not been reported to express TH or ChAT, we think it unlikely that they are a major contributor to the activation-induced phenotypes we observed, but we cannot completely rule out their involvement.

Exposure to the external environment charges the intestines with myriad responsibilities including absorption and digestion of dietary nutrients, exclusion of xenobiotics, protection from enteric infection, and partnership with the gut microbiome. Deletion of ChAT in enteric neurons leads to microbiome dysbiosis (Johnson et al., 2018), and we observed differences in the compositional profile (both metagenomic and proteomic) of the gut microbiome specific to activation of ChAT$^+$ neurons. Notably, we found an expansion of Verrucomicrobia driven by *A. muciniphila*, which has been implicated in human diseases such as obesity (Everard et al., 2013; Plovier et al., 2017), multiple sclerosis (Cekanaviciute et al., 2017; Jangi et al., 2016), and seizures (Olson et al., 2018). *A. muciniphila* metabolizes host-derived mucus as a nutrient source (Derrien et al., 2004; Van Herreweghen et al., 2017), consistent with the increase in luminal mucin proteins and digestive enzymes we observed in ChAT$^+$-activated mice. A particularly interesting host-microbial interaction emerged from activation of TH$^+$ cells, which led to a dramatic decrease in anti-fungal chitinase (CHIA) protein expression and a concomitant bloom in fungi, suggesting that neuronal circuits can regulate fungal populations in the gut. If validated, this would be a novel demonstration of a host-microbial interaction with implications for health. Our study does not, however, reveal the mechanism(s) by which ENS activation reshapes the gut microbial community structure, which may involve altered colonic motility, changes in mucus production, modulation of mucosal immune responses, and/or shifts in metabolism and nutrient availability.

The human gut microbiome possesses as much metabolic capacity as the liver; it is therefore no surprise that changes to both mouse gut physiology and the microbiome have major influences on the gut metabolome. In a striking example of mutualism, we report widespread changes to the pool of intestinal bile acids, molecules produced via host-microbial co-metabolism. Activation of ChAT$^+$ neurons, but not TH$^+$ neurons, impacted expression of NPC1L1, which is involved in cholesterol transport. In mammals, cholesterol is the substrate for production of primary bile acids, which are then metabolized exclusively by the gut microbiome into secondary bile acids. Bile acids play critical roles in fat absorption (de Aguiar Vallim et al.,

2013), gut motility (Kirwan et al., 1975), hormonal signaling (Watanabe et al., 2006) and immune functions (Fiorucci et al., 2018), and neurological conditions (McMillin and DeMorrow, 2016). Expression of bile salt hydrolases and hydratases increases the fitness of both commensal and pathogenic bacteria (Begley et al., 2005; Delpino et al., 2007; Hofmann and Eckmann, 2006; Jones et al., 2008; Sannasiddappa et al., 2017). While additional work is required to determine how the ENS affects levels and constitution of the bile acid pool, understanding the processes that regulate synthesis of secondary bile acids may have implications for organ systems throughout the body.

Our study complements recent single-cell RNAseq studies of the ENS neuronal transcriptome (Drokhlyansky et al., 2020) by giving us the ability to selectively activate specific enteric neurons and explore the dynamic interplay between cells of various lineages in the gut. Importantly, the transcriptomic changes we observed may be a consequence of direct or indirect effects of neuronal activation. Indeed, induced activation of $ChAT^+$ or TH^+ neurons rapidly changed GI transit and fluid secretion patterns, which are only a fraction of the processes that may feed back on epithelial or immune cells, altering their gene expression profiles. Further single-cell analysis may help dissect the roles of the various intestinal cells that collaborate to coordinate gut functions.

The ENS adapts and responds to incredibly diverse molecular cues from the environment and must do so throughout the entire length and surface area of the intestines—the largest and most extensive internal organ, with a rich network of neurons termed the “second brain” (Gershon, 2015). Exposure to molecules from the diet or the microbiome may modulate ENS function, along with signals from outside the gut such as the circulatory system. Curiously, many disorders of the brain are also associated with GI symptoms (Bhavsar et al., 2013; Cersosimo et al., 2013; Del Giudice et al., 1999; Pfeiffer, 2003; Valicenti-McDermott et al., 2008). While mechanisms linking the gut and the brain, and their consequences for health, are an active area of study, the impact of neuronal activation within the ENS has largely been unexplored. Herein, we establish an experimental system that allows controlled activation of intrinsic and extrinsic neurons of the gut, separated from inputs from the brain, and demonstrate broad changes in the gut environment and its physiology that differ by activated neuronal population. The extensive datasets on activation of two major gut-associated neuronal populations that we generated should serve as a resource for further studies on the interconnected biological systems governing the complex relationship between gut physiology and the microbiome. Future

deployment of this approach could enable mapping of neuronal connections into and out of the gut, providing insights into how the ENS networks with tissues throughout the body and advancing growing research into the many functions of the GI tract, an endeavor with important consequences for human health.

ACKNOWLEDGMENTS

We thank members of the Mazmanian laboratory for discussions throughout the research project and critical reading of the manuscript, and Dr. Catherine Oikonomou for invaluable manuscript editing. We thank Dr. Andres Collazo and Caltech's Biological Imaging Facility for training and access to microscopy capabilities and the Caltech Proteome Exploration Laboratory for access to LC-MS/MS capabilities. This research was funded in part by Aligning Science Across Parkinson's (ASAP-020495 and ASAP-000375) through the Michael J. Fox Foundation for Parkinson's Research (MJFF). For the purpose of open access, the authors have applied a CC BY 4.0 public copyright license to all Author Accepted Manuscripts arising from this submission. This work was also supported by grants to S.K.M. from the Heritage Medical Research Institute, Emerald Foundation, Caltech Center for Environmental and Microbial Interactions (CEMI), the National Institutes of Health (GM007616 and DK078938), and the Department of Defense (PD160030).

AUTHOR CONTRIBUTIONS

J.A.G., B.B.Y., and S.K.M. designed experiments. J.A.G. and B.B.Y. performed experiments. J.A.G., K.Y.C., and C.C. (supervised by V.G.) helped with AAV-mediated ENS characterization. P.T.B (supervised by D.W.W.), M.J.S., and A.M. performed acquisition and analysis of proteomic data. V.C., G.H., G.S., Q.Z., and J.S. (supervised by R.K.) performed acquisition and analysis of metagenomic data. K.W. (supervised by P.C.D.) performed acquisition and analysis of metabolomic data. T.M.T. assisted in animal-related work. J.A.G., B.B.Y., and S.K.M wrote the manuscript with input from all authors.

DECLARATION OF INTERESTS

The authors declare no financial or other interests directly related to this work

Figure 1

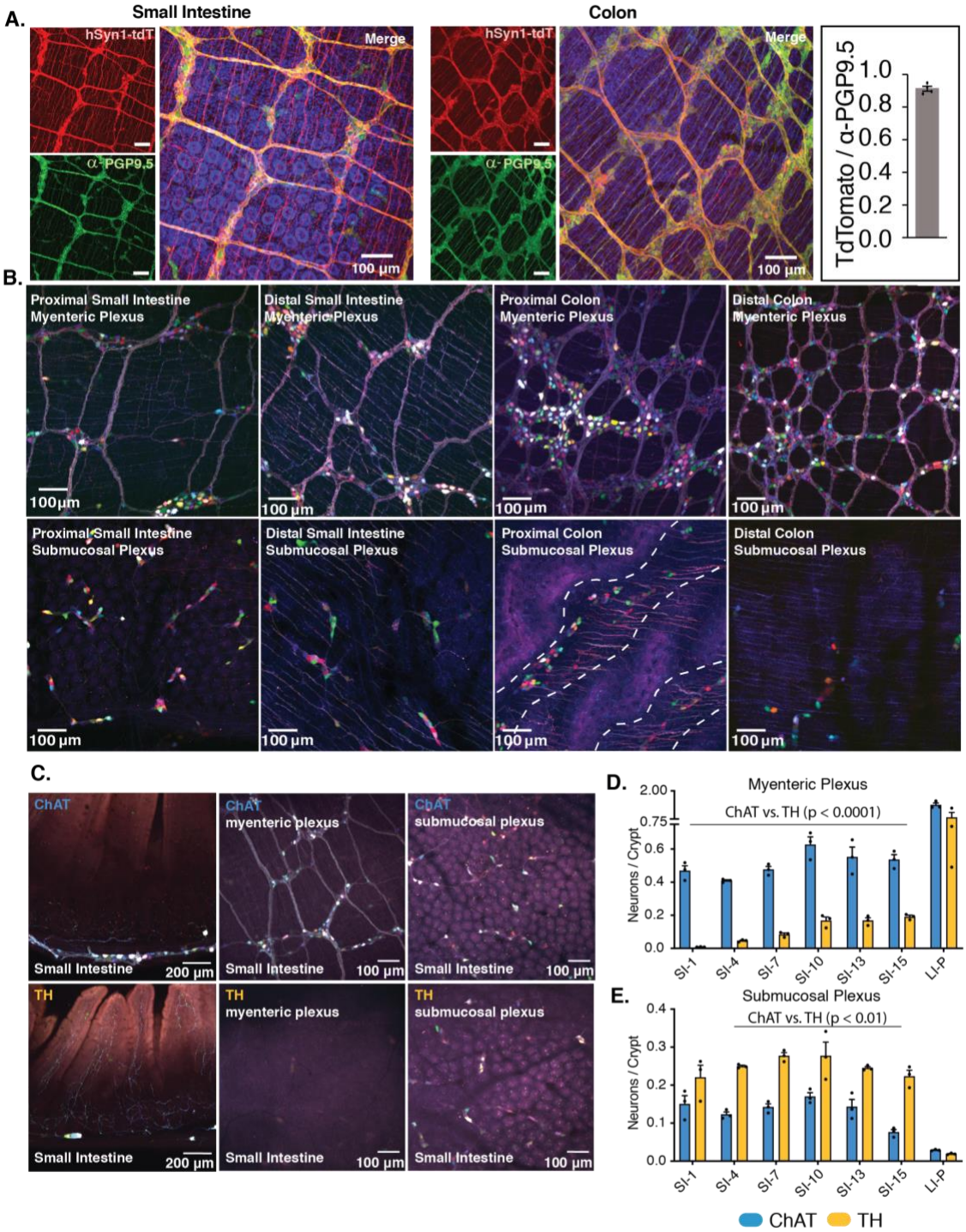
A.
Small Intestine
Colon
hSyn1-tdT
Merge
α-PGP9.5
100 µm
TdTomato / α-PGP9.5
1.0
0.8
0.6
0.4
0.2
0.0
B.
Proximal Small Intestine Myenteric Plexus
Distal Small Intestine Myenteric Plexus
Proximal Colon Myenteric Plexus
Distal Colon Myenteric Plexus
Proximal Small Intestine Submucosal Plexus
Distal Small Intestine Submucosal Plexus
Proximal Colon Submucosal Plexus
Distal Colon Submucosal Plexus
C.
ChAT
ChAT myenteric plexus
ChAT submucosal plexus
TH
TH myenteric plexus
TH submucosal plexus
Small Intestine
200 µm
D.
Myenteric Plexus
ChAT vs. TH (p < 0.0001)
Neurons / Crypt
SI-1
SI-4
SI-7
SI-10
SI-13
SI-15
LI-P
E.
Submucosal Plexus
ChAT vs. TH (p < 0.01)
ChAT
TH

Figure 1. ChAT$^+$ versus TH$^+$ Neuronal Distribution in the ENS

(A) Representative images of SI and colon from mice infected with AAV-PHP.S-hSYN1-tdTomato and immunolabelled with the pan-neuronal antibody PGP9.5. Inset shows quantification of the ratio of tdTomato$^+$ cells / PGP9.5$^+$ cells (N=3 mice, each data point represents the average of 3 representative fields).

(B) Representative images of proximal and distal regions of the SI and colon from AAV-PHP.S-hSYN1-XFP infected mice. Dotted lines demarcate the rugae (folds) in the proximal colon.

(C) Representative images of cross-sections, myenteric, and submucosal plexuses in ChAT-Cre and TH-Cre mice infected with AAV-PHP.S-hSYN1-DIO-XFP.

(D-E) Density of neurons in the myenteric plexus and submucosal plexus of ChAT-Cre and TH-Cre mice normalized to the number of crypts (N=3 mice, each data point represents the average of 3 representative fields).

See also Figures S1-S5 and Video Supplement 1

Source Data Figure 1

https://github.com/mazmanianlab/Griffiths_Yoo_et_al/tree/main/ENS%20quantification

Figure S1

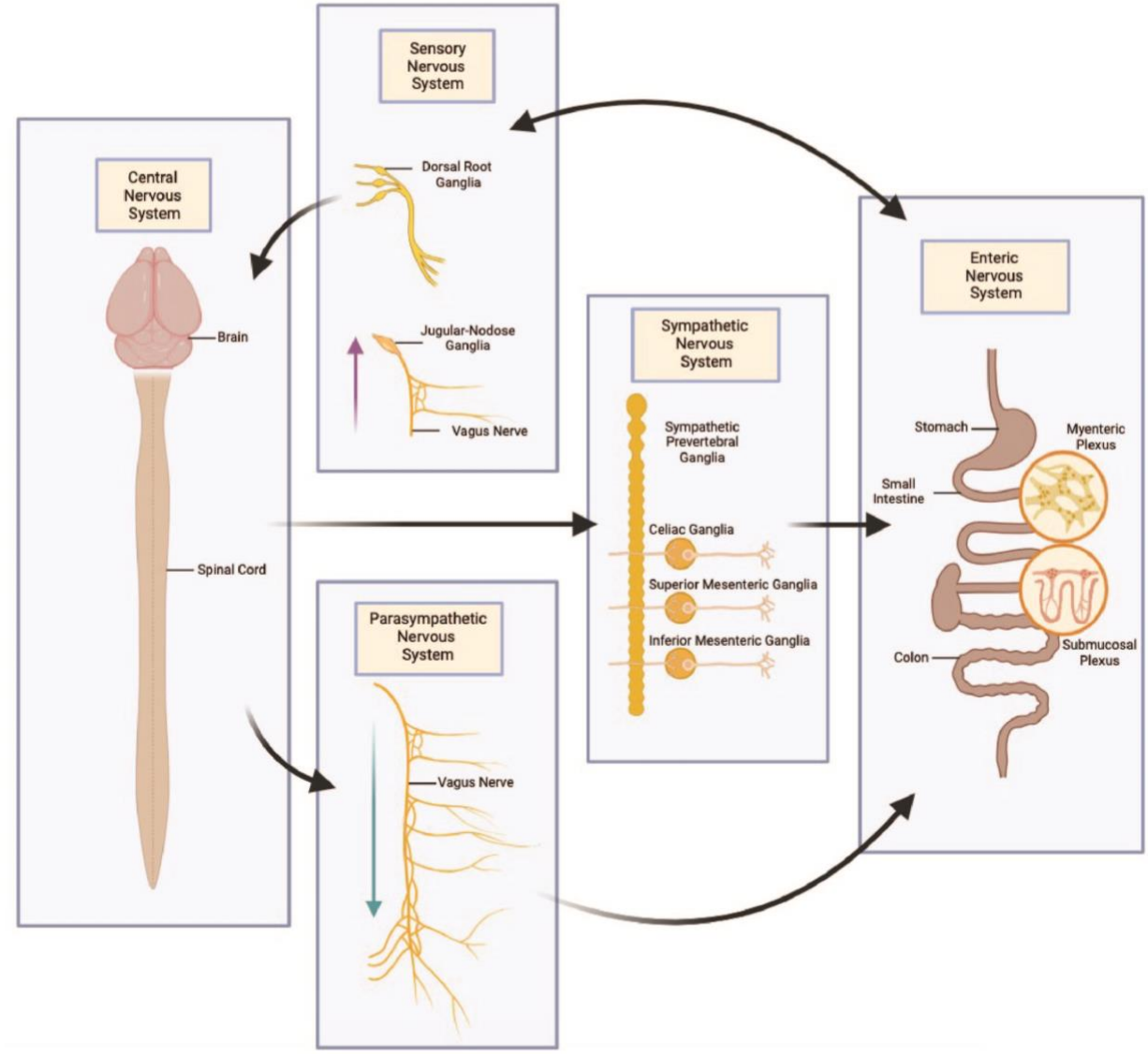
Sensory Nervous System
Dorsal Root Ganglia
Jugular-Nodose Ganglia
Vagus Nerve
Central Nervous System
Brain
Spinal Cord
Parasympathetic Nervous System
Vagus Nerve
Sympathetic Nervous System
Sympathetic Prevertebral Ganglia
Celiac Ganglia
Superior Mesenteric Ganglia
Inferior Mesenteric Ganglia
Enteric Nervous System
Stomach
Myenteric Plexus
Small Intestine
Colon
Submucosal Plexus

Figure S2. Extrinsic and Intrinsic Innervation of the GI Tract

Neurons of the sympathetic, parasympathetic, and sensory nervous systems extrinsically innervate the gut and have effects on GI function. In the sensory nervous system, sensory information from the gut is transmitted to the dorsal root ganglia (DRGs) and then to the spinal cord. Additionally, projections from the DRGs transmit sensory information to the gut. Other sensory signals arise from the periphery and are transmitted through the vagus nerve into the jugular-nodose ganglia and then into the brain. In the sympathetic nervous system, neurons from the spinal cord synapse onto neurons in the sympathetic prevertebral ganglia, celiac ganglia, superior mesenteric ganglia, and inferior mesenteric ganglia. These neurons then project to the gut. In the parasympathetic nervous system, the vagus nerve transmits signals from the brain to the gut. The intrinsic neurons of the gut, i.e., the enteric nervous system (ENS), reside in the myenteric and submucosal plexuses along the gut. Figure created with BioRender.com.

Figure S2

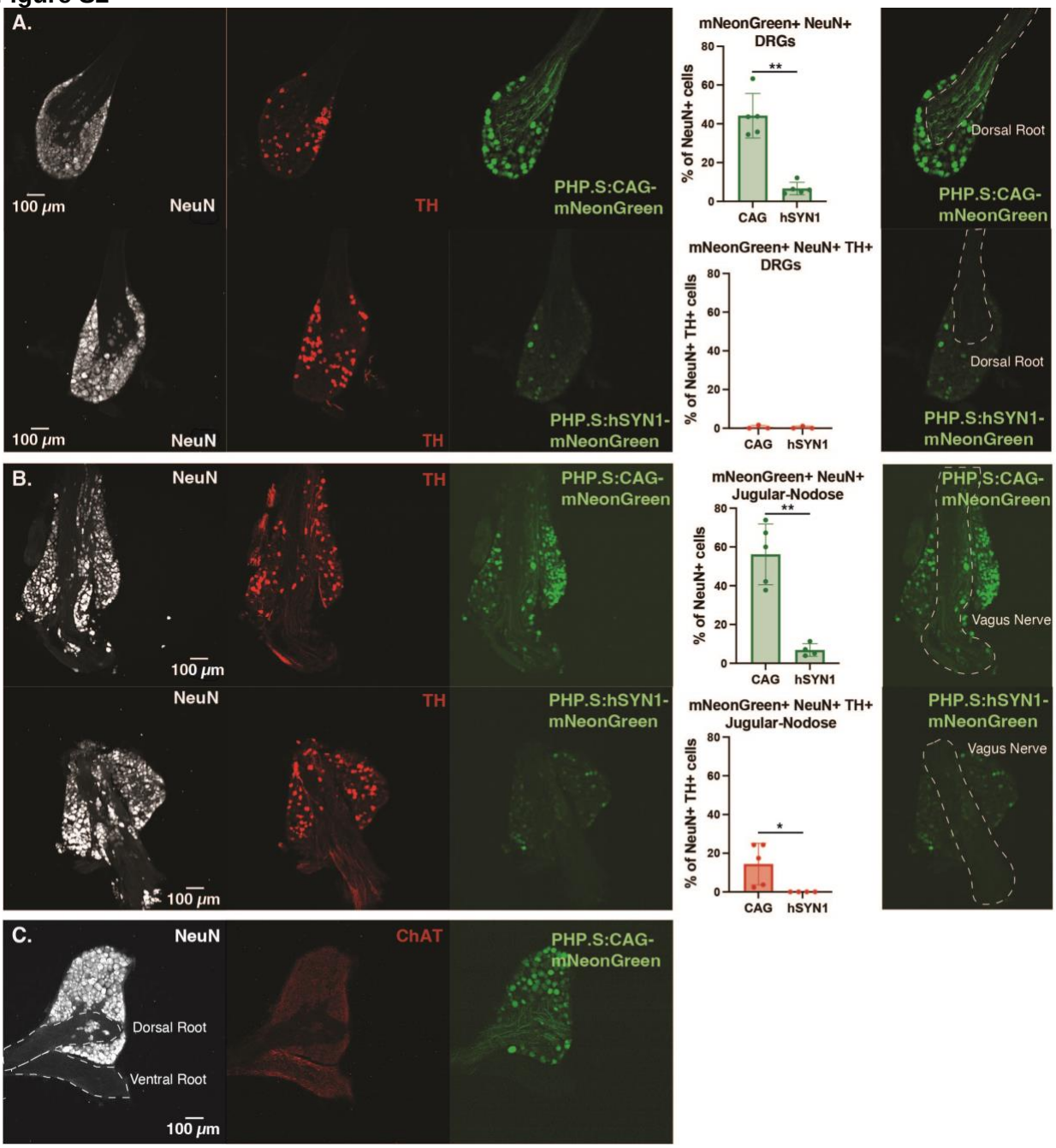
A.
100 μm
NeuN
TH
PHP.S:CAG-mNeonGreen
PHP.S:hSYN1-mNeonGreen
mNeonGreen+ NeuN+ DRGs
% of NeuN+ cells
CAG
hSYN1
Dorsal Root
mNeonGreen+ NeuN+ TH+ DRGs
% of NeuN+ TH+ cells
B.
mNeonGreen+ NeuN+ Jugular-Nodose
Vagus Nerve
mNeonGreen+ NeuN+ TH+ Jugular-Nodose
C.
ChAT
Dorsal Root
Ventral Root

Figure S2. Viral Transduction of the Peripheral Nervous System (PNS)

(A) Representative images showing labelling of the dorsal root ganglia (DRGs) by a single injection (10^{12} vg) of either PHP.S-CAG-mNeonGreen or PHP.S-hSYN1-mNeonGreen. Cryosections were immunostained for the neuronal marker NeuN and tyrosine hydroxylase (TH). Plots show quantification of NeuN+ cells and NeuN+ TH+ cells virally labelled by AAV-PHP.S-CAG vs. AAV-PHP.S-hSyn1 in DRGs. (N=3-5 mice, each data point represents a 40 µM medial cross-section of the DRG, **$p<0.01$, determined by Welch's two-tailed t-test)

(B) Representative images showing labelling of the jugular-nodose ganglia by a single injection (10^{12} vg) of either PHP.S-CAG-mNeonGreen or PHP.S-hSYN1-mNeonGreen. Cryosections were immunostained for the neuronal marker NeuN and TH. Plots show quantification of NeuN+ cells and NeuN+ TH+ cells virally labelled by AAV-PHP.S-CAG vs. AAV-PHP.S-hSyn1 in the jugular-nodose ganglia (N=4-5 mice, each data point represents a 40 µM medial cross-section of the jugular-nodose ganglia, **$p<0.01$, determined by Welch's two-tailed t-test).

(C) Representative images showing labelling of the dorsal root ganglia (DRGs), dorsal, and ventral root by a single injection (10^{12} vg) of PHP.S-CAG-mNeonGreen. Cryosections were immunostained for the neuronal marker NeuN and ChAT. ChAT staining shows expected ChAT+ projections in the ventral root, but not the dorsal root or intrinsic neurons of the DRGs.

Figure S3

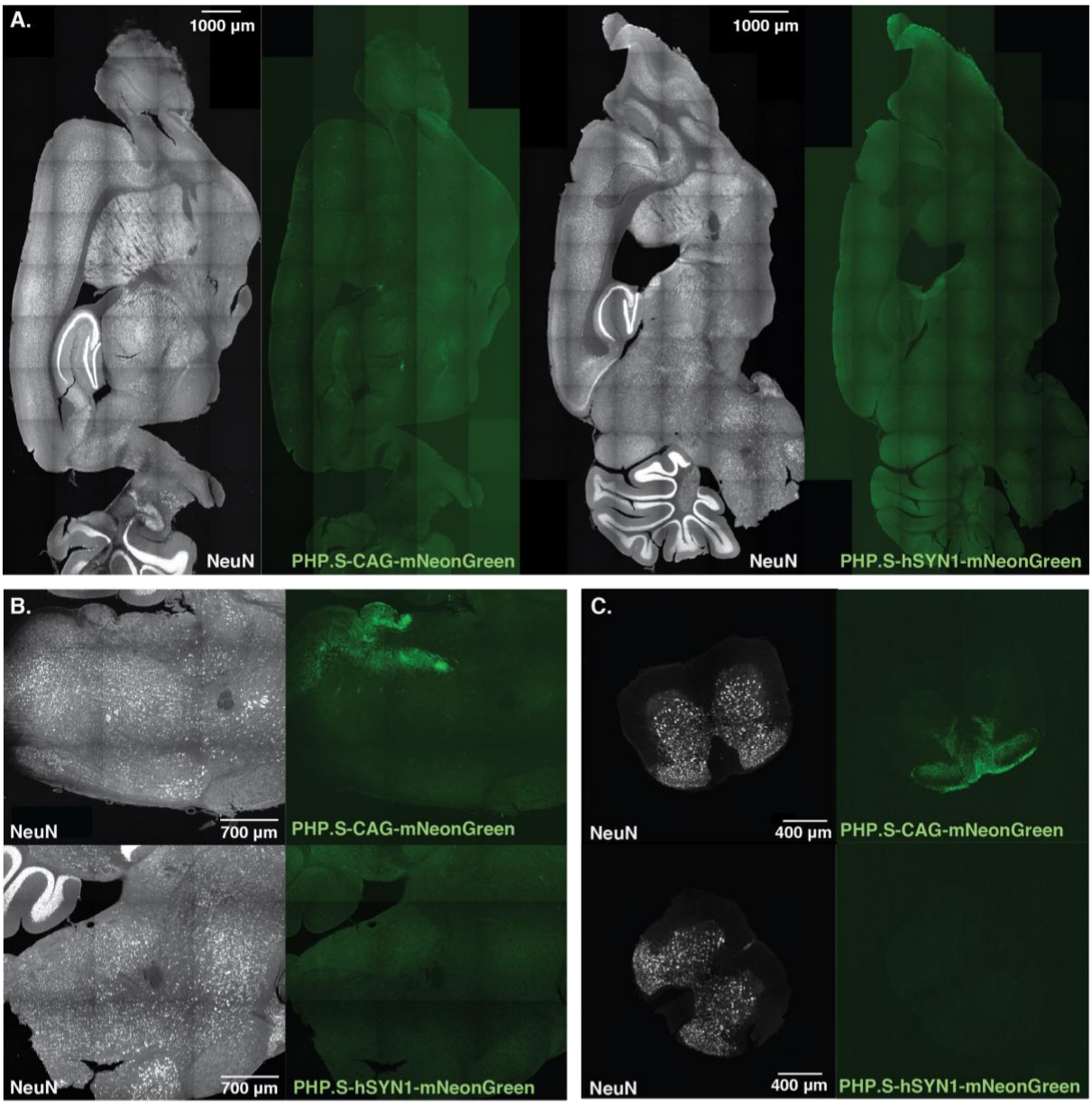
A.
1000 µm
NeuN
PHP.S-CAG-mNeonGreen
1000 µm
NeuN
PHP.S-hSYN1-mNeonGreen
B.
NeuN
700 µm
PHP.S-CAG-mNeonGreen
NeuN
700 µm
PHP.S-hSYN1-mNeonGreen
C.
NeuN
400 µm
PHP.S-CAG-mNeonGreen
NeuN
400 µm
PHP.S-hSYN1-mNeonGreen

Figure S3. Viral Transduction of the CNS by AAV-PHP.S

(A) Representative images showing labelling of the brain by a single injection (10^{12} vg) of either AAV-PHP.S-CAG-mNeonGreen or AAV-PHP.S-hSYN1-mNeonGreen. Sections were immunostained for the neuronal marker NeuN.

(B, C) The PHP.S-hSYN1 injected mice did not show detectable mNeonGreen+ projections in the (B) brainstem or (C) spinal cord as were seen in the PHP.S-CAG injected mice.

Figure S4

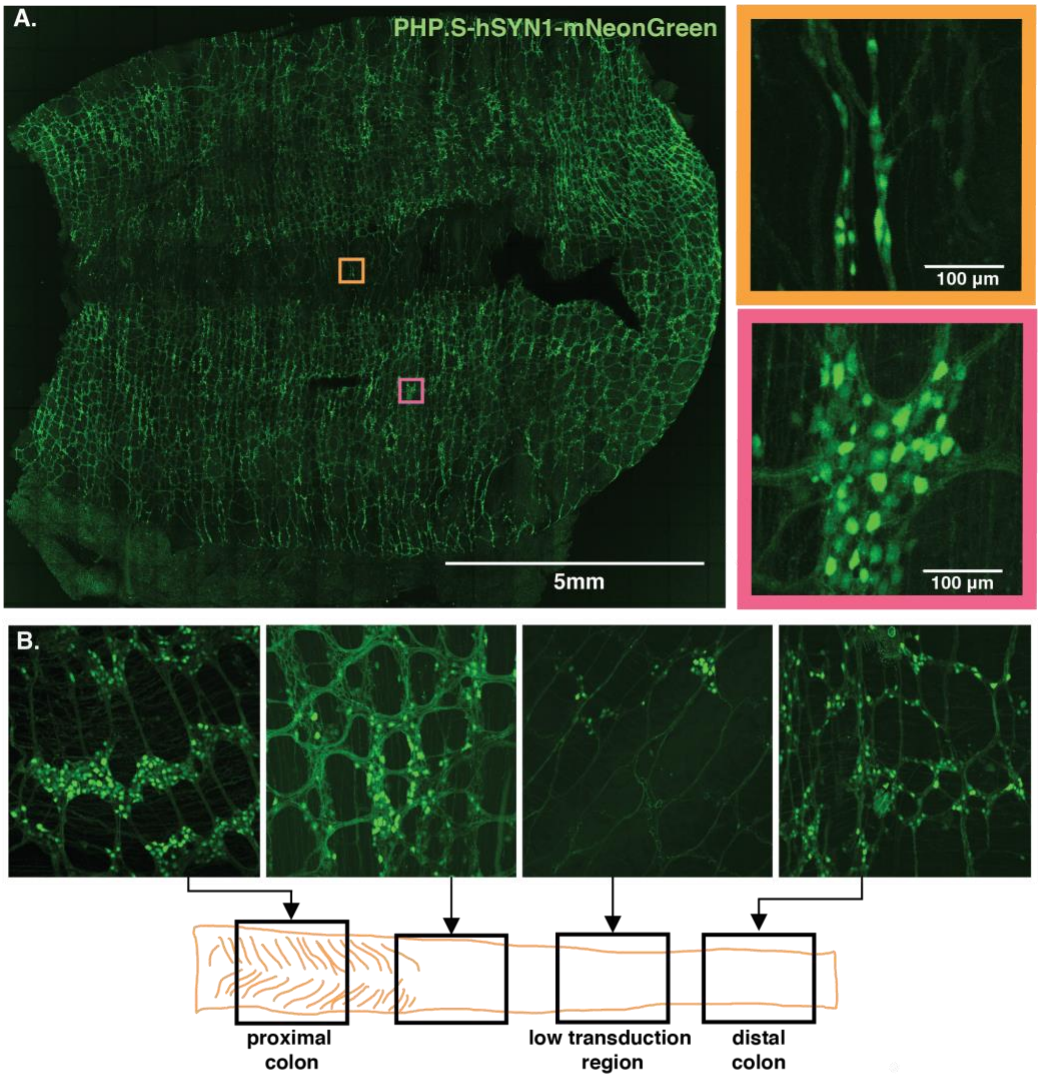
A.
PHP.S-hSYN1-mNeonGreen
5mm
100 µm
100 µm
B.
proximal colon
low transduction region
distal colon

Figure S4. Viral Transduction by AAV-PHP.S in the Colon

(A) Tiled, whole mount microscopy showing widespread labelling in the proximal colon (>1 cm of tissue) from a single injection of AAV-PHP.S-hSYN1-mNeonGreen (10^{12} vg). Orange inset highlights a region opposite the mesenteric attachment, and pink inset highlights a central region of the tissue.

(B) Representative images showing labelling patterns along the colon, including a 1.5 cm region that AAV-PHP.S does not transduce well.

Figure S5

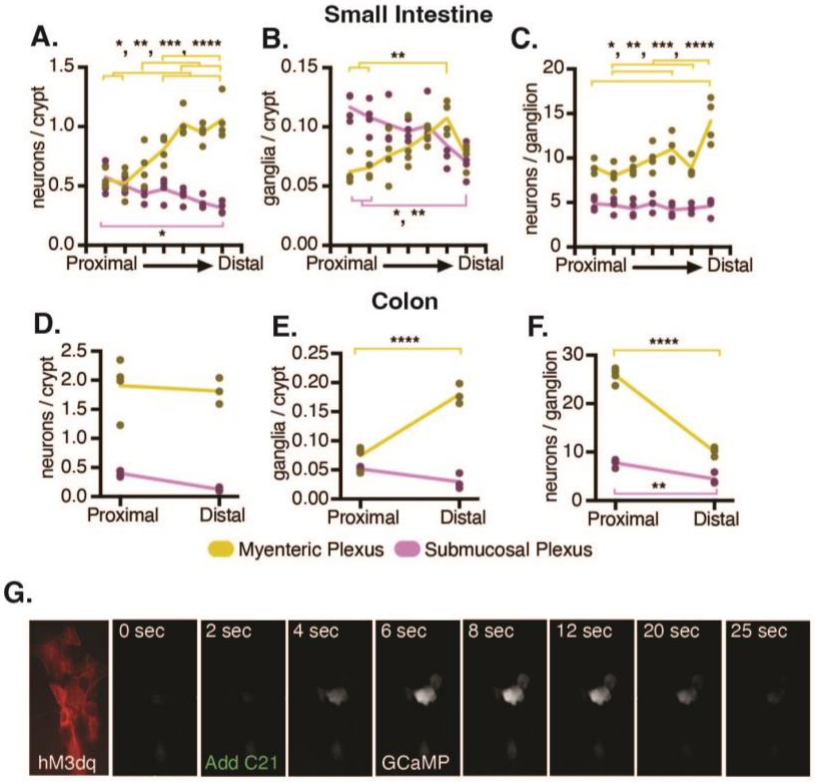
Small Intestine
A.
B.
C.
neurons / crypt
ganglia / crypt
neurons / ganglion
Proximal
Distal
Colon
D.
E.
F.
Myenteric Plexus
Submucosal Plexus
G.
0 sec
2 sec
4 sec
6 sec
8 sec
12 sec
20 sec
25 sec
hM3dq
Add C21
GCaMP

Figure S5. ENS Architecture and ChAT$^+$ Neuronal Stimulation in the ENS

(A-C) Quantification of neurons in 7 regions from the SI

(D-F) Quantification of neurons in 2 regions from the colon

(In A-F: N=3-4 mice per group, per intestinal region. Data points are averages from 2-3 images per mouse, per region; *: $p<0.05$, **: $p<0.01$, ***: $p<0.001$, ****: $p<0.0001$, determined by 2-way ANOVA with Sidak's multiple comparisons test)

(G) Fluorescence time course of GCaMP6f following C21 administration in an *ex vivo* preparation of ChAT$^+$ SI infected with hSYN1-DiO-hM3Dq-mRuby2 and CAG-GCaMP6f.

Figure 2

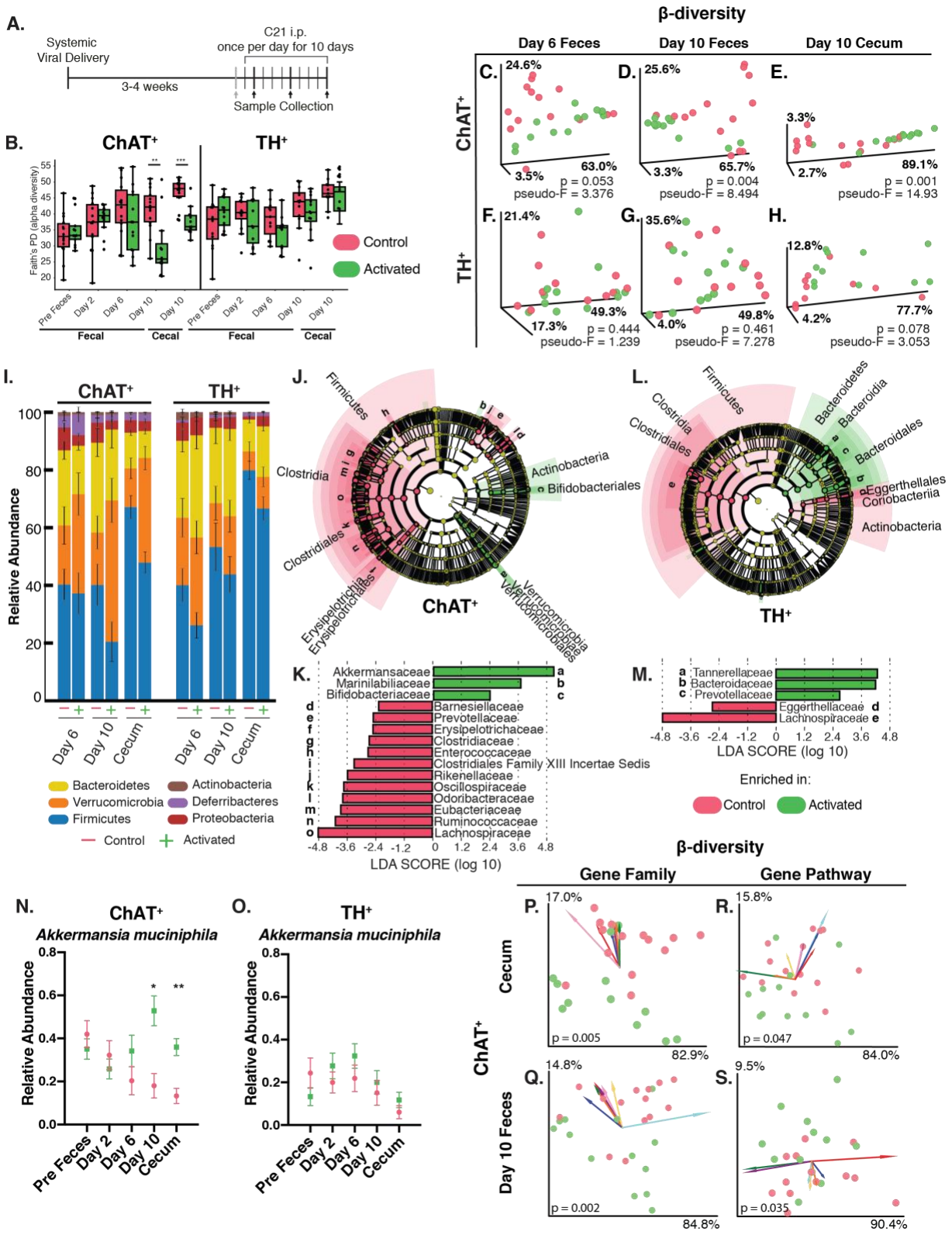
A.
Systemic Viral Delivery
C21 i.p. once per day for 10 days
3-4 weeks
Sample Collection
B.
ChAT+
TH+
Faith's PD (alpha diversity)
Control
Activated
Pre Feces
Day 2
Day 6
Day 10
Fecal
Cecal
β-diversity
Day 6 Feces
Day 10 Feces
Day 10 Cecum
C. 24.6% 3.5% 63.0% p = 0.053 pseudo-F = 3.376
D. 25.6% 3.3% 65.7% p = 0.004 pseudo-F = 8.494
E. 3.3% 2.7% 89.1% p = 0.001 pseudo-F = 14.93
F. 21.4% 17.3% 49.3% p = 0.444 pseudo-F = 1.239
G. 35.6% 4.0% 49.8% p = 0.461 pseudo-F = 7.278
H. 12.8% 4.2% 77.7% p = 0.078 pseudo-F = 3.053
I.
Relative Abundance
Day 6
Day 10
Cecum
Bacteroidetes
Verrucomicrobia
Firmicutes
Actinobacteria
Deferribacteres
Proteobacteria
Control
Activated
J.
Firmicutes
Clostridia
Clostridiales
Erysipelotrichia
Erysipelotrichales
Actinobacteria
Bifidobacteriales
Verrucomicrobia
Verrucomicrobiales
ChAT+
L.
Firmicutes
Clostridia
Clostridiales
Bacteroidetes
Bacteroidia
Bacteroidales
Eggerthellales
Coriobacteriia
Actinobacteria
TH+
K.
Akkermansaceae
Marinilabiliaceae
Bifidobacteriaceae
Barnesiellaceae
Prevotellaceae
Erysipelotrichaceae
Clostridiaceae
Enterococcaceae
Clostridiales Family XIII Incertae Sedis
Rikenellaceae
Oscillospiraceae
Odoribacteraceae
Eubacteriaceae
Ruminococcaceae
Lachnospiraceae
LDA SCORE (log 10)
M.
Tannerellaceae
Bacteroidaceae
Prevotellaceae
Eggerthellaceae
Lachnospiraceae
LDA SCORE (log 10)
Enriched in:
Control
Activated
N.
ChAT+
Akkermansia muciniphila
Relative Abundance
O.
TH+
Akkermansia muciniphila
Relative Abundance
Pre Feces
Day 2
Day 6
Day 10
Cecum
β-diversity
Gene Family
Gene Pathway
P. 17.0% p = 0.005 82.9%
R. 15.8% p = 0.047 84.0%
Q. 14.8% p = 0.002 84.8%
S. 9.5% p = 0.035 90.4%
Cecum
Day 10 Feces
ChAT+

Figure 2. Gut-Associated ChAT$^+$ and TH$^+$ Neuronal Activation Alters the Gut Microbiome

(A) Experimental paradigm: Cre-dependent hM3Dq was virally administered to either ChAT-Cre or TH-Cre mice. After 3-4 weeks of expression, C21 was injected daily for 10 days to induce specific neuronal activation. Feces were sampled the day prior to the first C21 injection and on days 2, 6, and 10 of C21 administration, and tissue and cecal contents were collected one hour after the last injection.

(B) Faith's phylogenetic diversity of feces and cecal contents over 10 days of neuronal activation in ChAT$^+$ and TH$^+$ mice. Feces were collected pre-experiment (1 day before first injection) and on day 2, 6, and 10. Cecal contents were collected at experimental endpoint on day 10.
(**$p<0.01$, ***$p<0.001$ determined by Kruskal-Wallis one-way ANOVA)

(C-H) Weighted UniFrac principle coordinate analysis (PCoA) of Activated vs. Control in ChAT$^+$ and TH$^+$ mice. Statistics performed in QIIME2 as in (Bolyen et al., 2019)

(I) Stacked bar graph showing phylum-level changes in relative abundance on day 6 and day 10 of injection for feces and day 10 for cecal contents

(J-M) Linear discriminant analysis (LDA) Effect Size (LEfSe) of the cecal microbiome. Cladograms showing differential phylogenetic clusters and family-level differences in activated and control (J,K) ChAT$^+$ and (L,M) TH$^+$ mice
(Cutoff: $\log_{10}$(LDA Score) > 2 or < -2)

(N-O) Changes in relative abundance of *Akkermansia muciniphila* in feces and cecal contents of (N) ChAT$^+$ and (O) TH$^+$ mice. (n=11-14 mice per group, per time point; red=Control, green=hM3Dq-Activated, *$p<0.05$, **$p<0.01$, determined by multiple t-tests with Holm-Sidak correction for multiple comparisons)

(P-S) Beta-diversity of bacterial gene families and pathways in the (P,R) cecum and (Q,S) post-9 feces of control and activated mice. The direction and length of arrows indicate their influence in separating control and activated groups. Colors represent gene families and pathways (annotated in Figure S7).

See also Figures S6 and S7

Source Data Figure 2

https://github.com/mazmanianlab/Griffiths_Yoo_et_al/tree/main/metagenomics

Figure S6

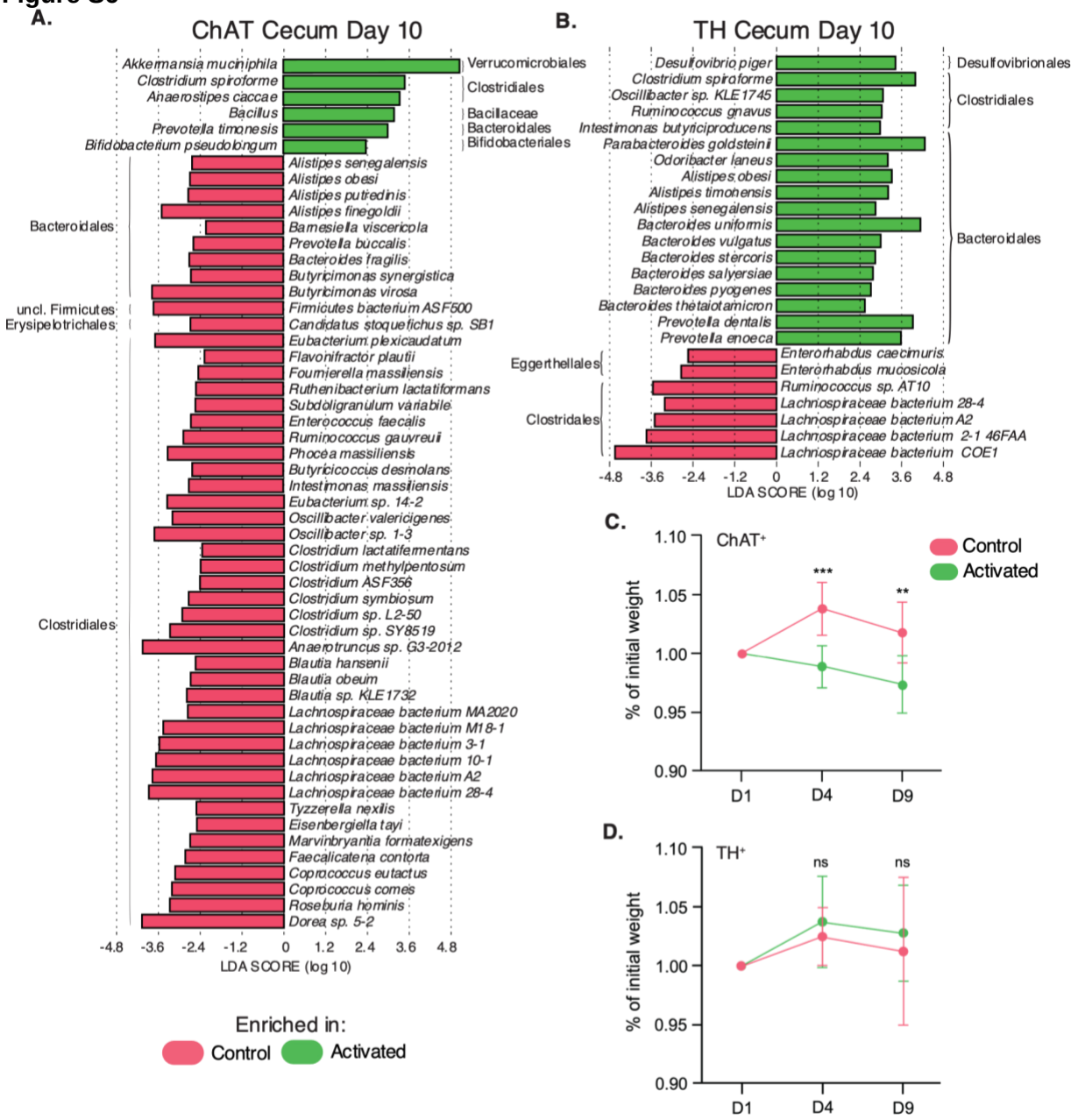
A.
ChAT Cecum Day 10
Akkermansia muciniphila
Clostridium spiroforme
Anaerostipes caccae
Bacillus
Prevotella timonesis
Bifidobacterium pseudolongum
Verrucomicrobiales
Clostridiales
Bacillaceae
Bacteroidales
Bifidobacteriales
Alistipes senegalensis
Alistipes obesi
Alistipes putredinis
Alistipes finegoldii
Bamesiella viscericola
Prevotella buccalis
Bacteroides fragilis
Butyricimonas synergistica
Butyricimonas virosa
Firmicutes bacterium ASF500
Candidatus stoquefichus sp. SB1
Eubacterium plexicaudatum
Flavonifractor plautii
Foumierella massiliensis
Ruthenibacterium lactatiformans
Subdoligranulum variabile
Enterococcus faecalis
Ruminococcus gauvreuii
Phocea massiliensis
Butyricicoccus desmolans
Intestimonas massiliensis
Eubacterium sp. 14-2
Oscillibacter valericigenes
Oscillibacter sp. 1-3
Clostridium lactatifermentans
Clostridium methylpentosum
Clostridium ASF356
Clostridium symbiosum
Clostridium sp. L2-50
Clostridium sp. SY8519
Anaerotruncus sp. G3-2012
Blautia hansenii
Blautia obeum
Blautia sp. KLE1732
Lachnospiraceae bacterium MA2020
Lachnospiraceae bacterium M18-1
Lachnospiraceae bacterium 3-1
Lachnospiraceae bacterium 10-1
Lachnospiraceae bacterium A2
Lachnospiraceae bacterium 28-4
Tyzzerella nexilis
Eisenbergiella tayi
Marvinbryantia formatexigens
Faecalicatena contorta
Coprococcus eutactus
Coprococcus comes
Roseburia hominis
Dorea sp. 5-2
Bacteroidales
uncl. Firmicutes
Erysipelotrichales
Clostridiales
-4.8 -3.6 -2.4 -1.2 0 1.2 2.4 3.6 4.8
LDA SCORE (log 10)
Enriched in:
Control
Activated
B.
TH Cecum Day 10
Desulfovibrio piger
Clostridium spiroforme
Oscillibacter sp. KLE1745
Ruminococcus gnavus
Intestimonas butyriciproducens
Parabacteroides goldsteinii
Odoribacter laneus
Alistipes obesi
Alistipes timonensis
Alistipes senegalensis
Bacteroides uniformis
Bacteroides vulgatus
Bacteroides stercoris
Bacteroides salyersiae
Bacteroides pyogenes
Bacteroides thetaiotaomicron
Prevotella dentalis
Prevotella enoeca
Enterorhabdus caecimuris
Enterorhabdus mucosicola
Ruminococcus sp. AT10
Lachnospiraceae bacterium 28-4
Lachnospiraceae bacterium A2
Lachnospiraceae bacterium 2-1 46FAA
Lachnospiraceae bacterium COE1
Desulfovibrionales
Clostridiales
Bacteroidales
Eggerthellales
Clostridales
-4.8 -3.6 -2.4 -1.2 0 1.2 2.4 3.6 4.8
LDA SCORE (log 10)
C.
ChAT+
Control
Activated
% of initial weight
1.10
1.05
1.00
0.95
0.90
***
**
D1 D4 D9
D.
TH+
ns
ns
% of initial weight
1.10
1.05
1.00
0.95
0.90
D1 D4 D9

Figure S6. Annotated changes in gut bacteria (Related to Figure 2 and Figure 6)

(A,B) Species-levels differences in cecal bacteria after 10 days of C21 injection in (A) $ChAT^+$ and (B) TH^+ mice

(C,D) Analysis of activation-mediated changes in body weight of (C) $ChAT^+$ and (D) TH^+ mice over 9 days of C21 administration

(N = 10-11 mice per group; **: $p<0.01$, ***: $p<0.001$, determined by 2-way ANOVA with Sidak's method for multiple comparisons)

Figure S7

A.

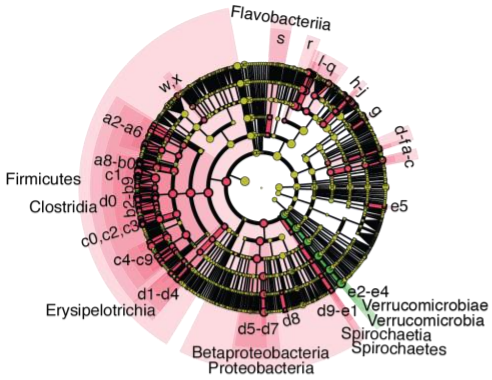

B.

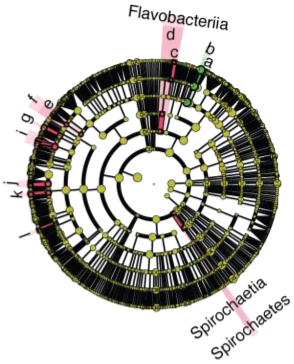

ChAT-Cre Day 10 Feces							
ID	Microbial Taxon	ID	Microbial Taxon	ID	Microbial Taxon	ID	Microbial Taxon
a	Bifidobacterium	p	Parabacteroides	b4	Dorea	d0	Clostridiales
b	Bifidobacteriaceae	q	Tannerellaceae	b5	Eisenbergiella	d1	Candidatus Stoquefichus
c	Bifidobacteriales	r	Marinilbiliales	b6	Faecalicatena	d2	Faecalitalea
d	Cellulomonas	s	Flavobacteriales	b7	Lachnoclostridium	d3	Erysipelotrichaeceae
e	Cellulomondaceae	w	Enterococcus	b8	Marvinbryantia	d4	Erysipelotrichales
f	Micrococcales	x	Enterococcaceae	b9	Sellimonas	d5	Parasutterella
g	Adlercreutzia	a2	Intestinimonas	c0	Tyzzerella	d6	Sutterellaceae
h	Barnsiella	a3	Pseudoflavonifractor	c1	Lachnospiraceae	d7	Burkholderiales
i	Coprobacter	a5	Clostridium	c2	Oscillibacter	d8	Lawsonia
j	Barnesiellaceae	a6	Clostridiaceae	c3	Oscillospiraceae	d9	Treponema
k	Prevotella	a8	Anaerofustis	c5	Anaerotruncus	e0	Spirochaetaceae
l	Prevotellaceae	a9	Eubacterium	c6	Ruminiclostridium	e1	Spirochaetales
m	Alistipes	b0	Eubacteriaceae	c7	Ruminococcus	e2	Akkermansia
n	Rikenella	b2	Blautia	c8	Ruthenibacterium	e3	Akkermansiaceae
o	Rikenellaceae	b3	Coprococcus	c9	Ruminococaceae	e4	Verrucomicrobiales
						e5	Varicellovirus

TH-Cre Day 6 Feces	
ID	Microbial Taxon
a	Parabacteroides
b	Tannerellaceae
c	Fluviicola
d	Flavobacteriales
e	Streptococcus
f	Streptococcaceae
g	Pseudoflavonifractor
i	Clostridium
j	Blautia
k	Eisenbergiella
l	Clostridiodes

Enriched in:
- Control
- Activated

C.

ChAT-Cre Cecum		
ID	Gene Family	Annotation
1	K02003	putative ABC transport system ATP-binding protein
2	K02518	translation initiation factor IF-1
3	K02948	small subunit ribosomal protein S11
4	K02950	small subunit ribosomal protein S12
5	K02965	small subunit ribosomal protein S19
6	K03205	type IV secretion system protein VirD4
7	K03294	basic amino acid/polyamine antiporter, APA family
8	K03496	chromosome partitioning protein
ID	**Gene Pathway**	**Annotation**
1	HISDEG-PWY	L-histidine degradation I
2	ILEUSYN-PWY	L-isoleucine biosynthesis I (from threonine)
3	PWY-6122	5-aminoimidazole ribonucleotide biosynthesis II
4	PWY-6595	superpathway of guanosine nucleotides degradation (plants)
5	PWY-6606	guanosine nucleotides degradation II
6	PWY-7111	pyruvate fermentation to isobutanol (engineered)
7	PWY-7219	adenosine ribonucleotides de novo biosynthesis
8	VALSYN-PWY	L-valine biosynthesis

D.

ChAT-Cre Day 10 Feces		
ID	Gene Family	Annotation
1	K02003	putative ABC transport system ATP-binding protein
2	K02518	translation initiation factor IF-1
3	K02913	large subunit ribosomal protein L33
4	K02946	small subunit ribosomal protein S10
5	K02948	small subunit ribosomal protein S11
6	K02950	small subunit ribosomal protein S12
7	K02965	small subunit ribosomal protein S19
8	K03205	type IV secretion system protein VirD4
ID	**Gene Pathway**	**Annotation**
1	ILEUSYN-PWY	L-isoleucine biosynthesis I (from threonine)
2	PWY-6151	S-adenosyl-L-methionine cycle I
3	PWY-6700	queuosine biosynthesis I (de novo)
4	PWY-6859	all-trans-farnesol biosynthesis
5	PWY-7111	pyruvate fermentation to isobutanol
6	PWY-7219	adenosine ribonucleotides de novo biosynthesis
7	PWY0-1296	purine ribonucleosides degradation
8	VALSYN-PWY	L-valine biosynthesis

Figure S7. Gut-Associated Activation-Mediated Changes in the Fecal Microbiome (Related to Figure 2)

(A) LEfSe cladograms and annotations for feces on Day 10 of C21 administration in $ChAT^+$ mice

(B) LEfSe Cladograms and annotations for feces on Day 6 of C21 administration in TH^+ mice

(C-D) Microbial gene family and pathway annotations for the feature arrows in Figures 2P-2S. Colors in the ID column refer to the colors of the arrows in the main figure.

Figure 3

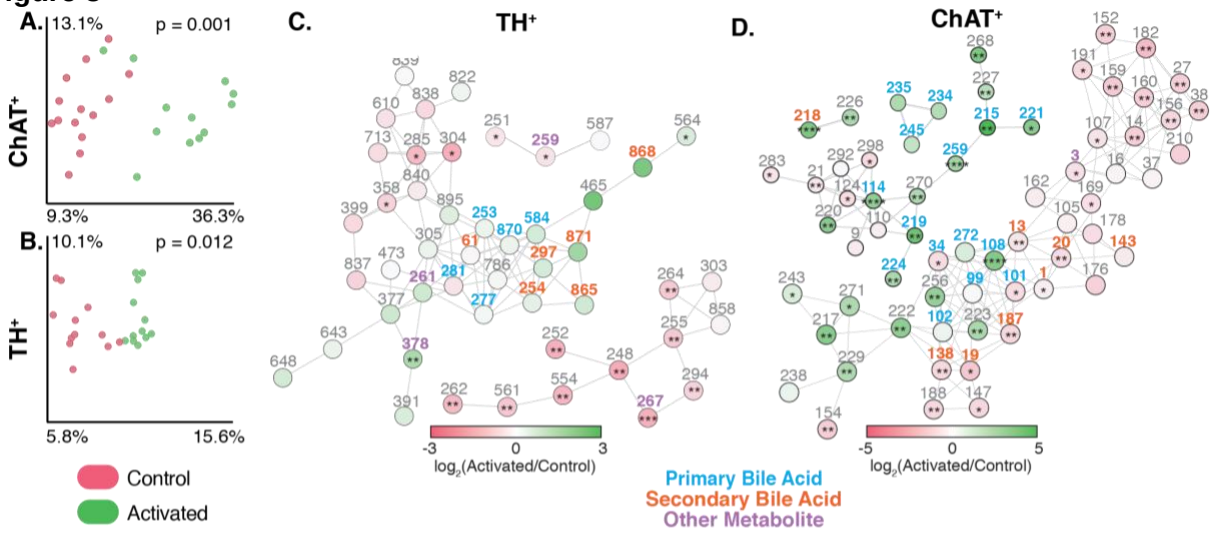

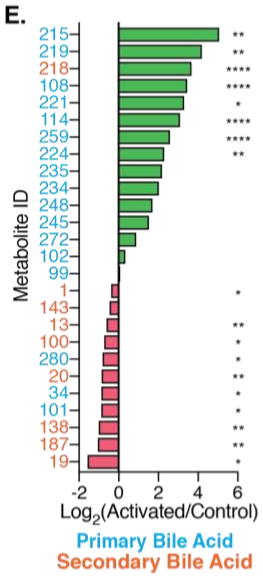

F.

ChAT+ Cecum

Activated > Control			Activated < Control		
ID	GNPS Annotation	Adduct	ID	GNPS Annotation	Adduct
215	Cholic acid	2M+H	19	Spectral Match to 12-Ketodeoxycholic acid (NIST14)	M+H
219	Cholic acid	2M+Na	187	hyocholic acid	M-2H2O+H
218	7-Keto-3.alpha.,12-.alpha.-dihydroxycholanic acid	M+H-3H2O	138	Spectral Match to 12-Ketodeoxycholic acid (NIST14)	M+H
108	Cholic acid	M-3H2O+H	101	.beta.-Muricholic acid	M+H-3H2O
221	Cholic acid	3M+H	34	3.alpha.-Hydroxy-7-oxo-5.beta.-cholanic acid	M+H-H2O
114	Cholic acid	M+Na	20	.alpha.-Hyodeoxycholic acid methyl ester	M+H-CH6O2
259	Cholic Acid	[M+NH4]+	280	.gamma.-Muricholic acid/hyocholic acid	M+H-H2O
224	Cholic acid	3M+Na	100	Spectral Match to Deoxycholic acid (NIST14)	2M+H
235	taurohyocholic acid	M+H	13	Spectral Match to Ursodeoxycholic acid (NIST14)	M+H-H2O
234	Spectral Match to Taurocholic acid (NIST14)	M+H	143	.beta.-Hyodeoxycholic acid	M+H-H2O
248	Spectral Match to Taurocholic acid (NIST14)	M+Na	1	.beta.-Hyodeoxycholic acid	M+H-2H2O
245	taurohyocholic acid	M-2H2O+H			
272	Spectral Match to Cholic acid (NIST14)	M+H-2H2O			
102	.beta.-Muricholic acid	M+H-H2O			
99	hyocholic acid	M-2H2O+H			

Primary Bile Acid
Secondary Bile Acid

Figure 3. Gut-Associated ChAT$^+$ or TH$^+$ Neuronal Activation Alters Host and Microbe-Derived Luminal Metabolites

(A-B) Canberra PCoA of the cell-free, luminal metabolome of cecal contents from control (red) and activated (green) ChAT$^+$ and TH$^+$ mice. Statistical analyses were performed in QIIME2 as in (Bolyen et al., 2019).

(C-D) Metabolic networks constructed from identified cecal metabolites in TH$^+$ and ChAT$^+$ mice. Each node is colored by its upregulation (green) or downregulation (red) in the activated group and is labelled with an ID number corresponding to annotation, mass-to-charge ratio, retention time, fold change, and significance value in Table S1.

(E) Fold changes of specific bile acids identified as upregulated (green bars) or downregulated (red bars) in activated ChAT$^+$ mice

(F) Annotations of bile acids highlighted in (E). Metabolite IDs are colored according to annotation as primary (blue) or secondary (orange) bile acids. Metabolite IDs are specific to each sample (N=12-14 for each group analyzed, *: $p<0.05$, **: $p<0.01$, ***: $p<0.001$, ****: $p<0.0001$)

See also Table S1

Figure 4

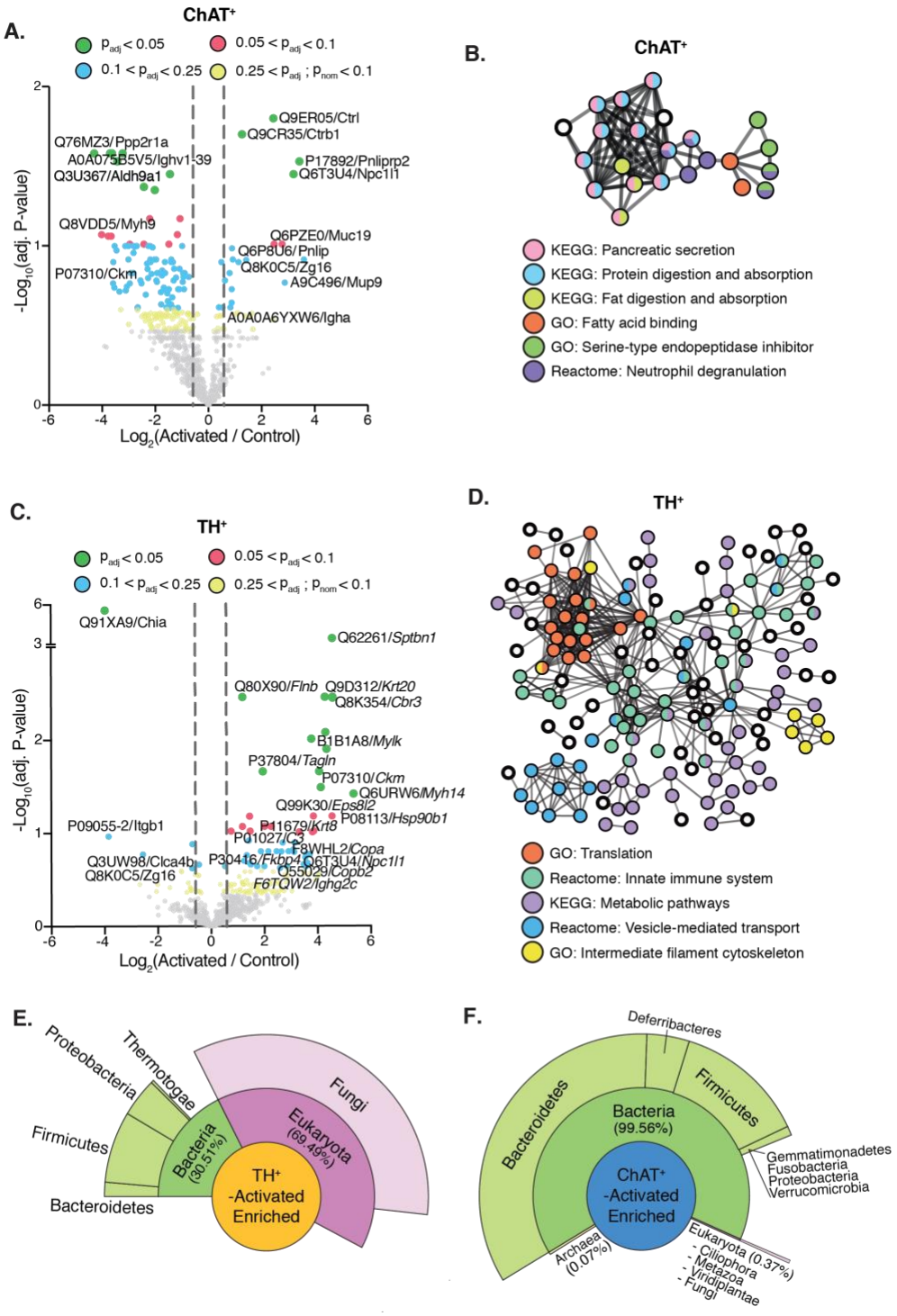
A.
ChAT+
$p_{adj} < 0.05$
$0.05 < p_{adj} < 0.1$
$0.1 < p_{adj} < 0.25$
$0.25 < p_{adj}$; $p_{nom} < 0.1$
Q9ER05/Ctrl
Q9CR35/Ctrb1
Q76MZ3/Ppp2r1a
A0A075B5V5/Ighv1-39
Q3U367/Aldh9a1
P17892/Pnliprp2
Q6T3U4/Npc1l1
Q8VDD5/Myh9
Q6PZE0/Muc19
Q6P8U6/Pnlip
Q8K0C5/Zg16
P07310/Ckm
A9C496/Mup9
A0A0A6YXW6/Igha
-Log10(adj. P-value)
Log2(Activated / Control)
B.
ChAT+
KEGG: Pancreatic secretion
KEGG: Protein digestion and absorption
KEGG: Fat digestion and absorption
GO: Fatty acid binding
GO: Serine-type endopeptidase inhibitor
Reactome: Neutrophil degranulation
C.
TH+
$p_{adj} < 0.05$
$0.05 < p_{adj} < 0.1$
$0.1 < p_{adj} < 0.25$
$0.25 < p_{adj}$; $p_{nom} < 0.1$
Q91XA9/Chia
Q62261/Sptbn1
Q80X90/Flnb
Q9D312/Krt20
Q8K354/Cbr3
B1B1A8/Mylk
P37804/Tagln
P07310/Ckm
Q6URW6/Myh14
Q99K30/Eps8l2
P08113/Hsp90b1
P09055-2/Itgb1
P11679/Krt8
P01027/C3
F8WHL2/Copa
Q3UW98/Clca4b
P30416/Fkbp4
Q6T3U4/Npc1l1
Q8K0C5/Zg16
O55029/Copb2
F6TQW2/Ighg2c
-Log10(adj. P-value)
Log2(Activated / Control)
D.
TH+
GO: Translation
Reactome: Innate immune system
KEGG: Metabolic pathways
Reactome: Vesicle-mediated transport
GO: Intermediate filament cytoskeleton
E.
Proteobacteria
Thermotogae
Fungi
Firmicutes
Bacteria (30.51%)
Eukaryota (69.49%)
TH+ -Activated Enriched
Bacteroidetes
F.
Deferribacteres
Bacteroidetes
Firmicutes
Bacteria (99.56%)
ChAT+ -Activated Enriched
Gemmatimonadetes
Fusobacteria
Proteobacteria
Verrucomicrobia
Archaea (0.07%)
Eukaryota (0.37%)
- Ciliophora
- Metazoa
- Viridiplantae
- Fungi

Figure 4. Gut-Associated ChAT$^+$ or TH$^+$ Neuronal Activation Alters Host and Microbe-Derived Luminal Proteins

(A) Volcano plot of differentially-expressed host proteins identified in the cecal contents of ChAT$^+$-activated (N=8) vs. ChAT$^+$-control mice (N=9) mice, 1 hour after final C21 administration

(B) STRING network analysis of host proteins that were more abundant in ChAT+-activated mice ($p_{nom.}$< 0.2)

(C) Proteomic volcano plot of TH$^+$-activated vs. TH$^+$-control mice (N=7 mice per group)

(D) STRING network analysis of upregulated host proteins in TH$^+$-activated mice ($p_{nom.}$< 0.2).

(E-F) Unipept metaproteomic analysis of upregulated microbial proteins (fold change > 2, $p_{nom.}$< 0.2) in TH$^+$-activated and ChAT$^+$-activated mice (N=7-9 mice per group)

Source Data Figure 4A

https://github.com/mazmanianlab/Griffiths_Yoo_et_al/blob/main/proteomics/CHAT_proteomics_volcano.txt

Source Data Figure 4C

https://github.com/mazmanianlab/Griffiths_Yoo_et_al/blob/main/proteomics/TH_proteomics_volcano.txt

Source Data Figures 4E and 4F

https://github.com/mazmanianlab/Griffiths_Yoo_et_al/blob/main/proteomics/metaproteomics/Microbiome_associated_proteins.xlsx

Figure 5

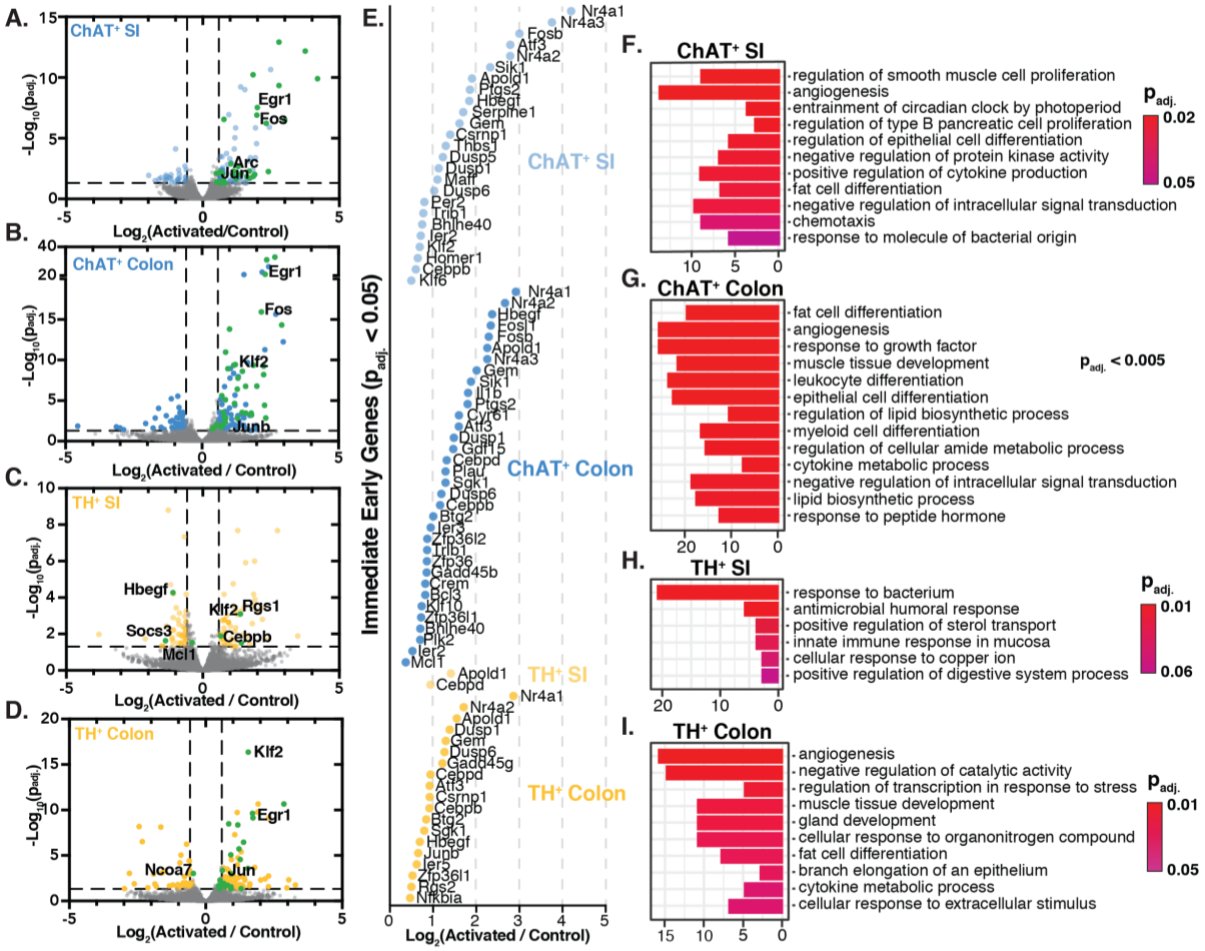
A.
ChAT+ SI
Egr1
Fos
Arc
Jun
Log2(Activated/Control)
B.
ChAT+ Colon
Egr1
Fos
Klf2
Junb
Log2(Activated / Control)
C.
TH+ SI
Hbegf
Klf2
Rgs1
Socs3
Cebpb
Mcl1
Log2(Activated / Control)
D.
TH+ Colon
Klf2
Egr1
Ncoa7
Jun
Log2(Activated / Control)
E.
Immediate Early Genes (padj. < 0.05)
ChAT+ SI
ChAT+ Colon
TH+ SI
TH+ Colon
Log2(Activated / Control)
F.
ChAT+ SI
regulation of smooth muscle cell proliferation
angiogenesis
entrainment of circadian clock by photoperiod
regulation of type B pancreatic cell proliferation
regulation of epithelial cell differentiation
negative regulation of protein kinase activity
positive regulation of cytokine production
fat cell differentiation
negative regulation of intracellular signal transduction
chemotaxis
response to molecule of bacterial origin
padj.
0.02
0.05
G.
ChAT+ Colon
fat cell differentiation
angiogenesis
response to growth factor
muscle tissue development
leukocyte differentiation
epithelial cell differentiation
regulation of lipid biosynthetic process
myeloid cell differentiation
regulation of cellular amide metabolic process
cytokine metabolic process
negative regulation of intracellular signal transduction
lipid biosynthetic process
response to peptide hormone
padj. < 0.005
H.
TH+ SI
response to bacterium
antimicrobial humoral response
positive regulation of sterol transport
innate immune response in mucosa
cellular response to copper ion
positive regulation of digestive system process
padj.
0.01
0.06
I.
TH+ Colon
angiogenesis
negative regulation of catalytic activity
regulation of transcription in response to stress
muscle tissue development
gland development
cellular response to organonitrogen compound
fat cell differentiation
branch elongation of an epithelium
cytokine metabolic process
cellular response to extracellular stimulus
padj.
0.01
0.05

Figure 5. ChAT$^+$ and TH$^+$ Activation-Mediated Transcriptomic Changes

(A-D) Differentially-expressed genes in DREADD-activated vs. control (A) ChAT$^+$ distal SI, (B) ChAT$^+$ proximal colon, (C) TH$^+$ distal SI, (D) TH$^+$ proximal colon
(Dashed vertical lines: Fold Change (FC) = +/- 1.5; dashed horizontal lines: $p_{adj.} < 0.05$. Transcripts of IEGs are highlighted in green and annotated. N=10 mice per group)
(E) Fold changes of upregulated IEGs ($p_{adj.} < 0.05$) as defined by Wu et al., 2017
(F-I) Gene set enrichment analysis of gene ontology (GO) terms for (F) ChAT$^+$ distal SI, (G) ChAT$^+$ proximal colon, (H) TH$^+$ distal SI, (I) TH$^+$ proximal colon.
See also Table S2 and Table S3

Source Data Figure 5

https://github.com/mazmanianlab/Griffiths_Yoo_et_al/tree/main/RNAseq

Figure 6

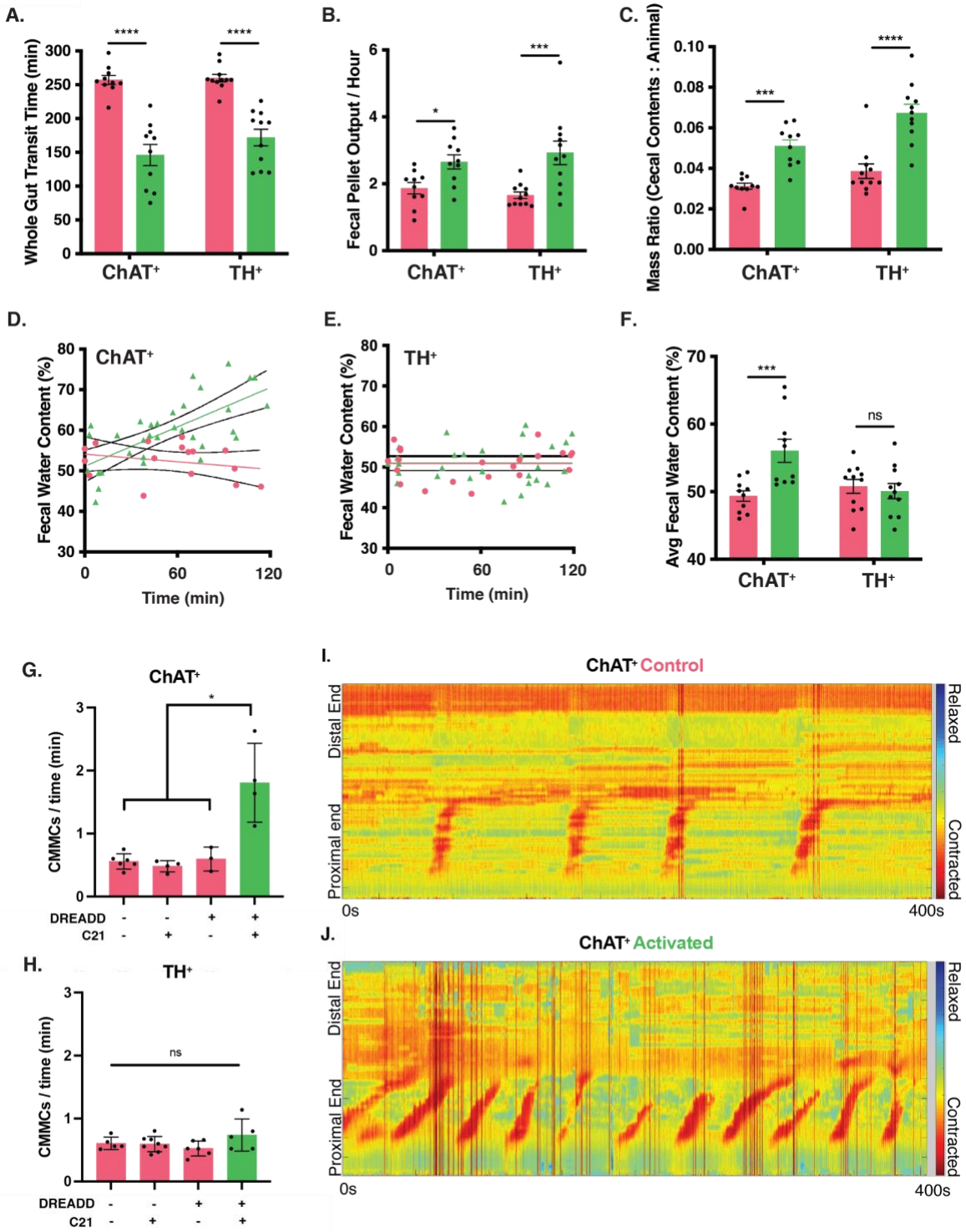
A.
Whole Gut Transit Time (min)
ChAT+
TH+
B.
Fecal Pellet Output / Hour
C.
Mass Ratio (Cecal Contents : Animal)
D.
ChAT+
Fecal Water Content (%)
Time (min)
E.
TH+
F.
Avg Fecal Water Content (%)
ns
G.
ChAT+
CMMCs / time (min)
DREADD
C21
H.
TH+
I.
ChAT+ Control
Distal End
Proximal end
Relaxed
Contracted
0s
400s
J.
ChAT+ Activated

Figure 6. GI Physiology Differences in ChAT$^+$ vs. TH$^+$ mice Following Activation

(A) Activation-mediated changes in whole gut transit time in ChAT$^+$ and TH$^+$ mice
(B) Activation-mediated changes in fecal pellet output in ChAT$^+$ and TH$^+$ mice
(C) Activation-mediated changes in normalized cecal content mass in ChAT$^+$ and TH$^+$ mice
(D-E) Fecal pellet water content in (D) ChAT$^+$ and (E) TH$^+$ mice over 2 hours following C21 activation
(F) Average fecal pellet water content in ChAT$^+$ and TH$^+$ mice following activation
(A-F: N = 10-11 mice per group; *: $p<0.05$, ***: $p<0.001$, ****: $p<0.0001$, determined by 2-way ANOVA with Sidak's method for multiple comparisons)
(G-H) Frequency of *ex vivo* CMMCs from (G) ChAT$^+$ and (H) TH$^+$ mice over 30 minutes following activation
(N = 3-8 mice per group; *: $p<0.05$, determined by 2-way ANOVA with Sidak's method for multiple comparisons)
(I-J) Heatmaps showing frequency of CMMCs over 400 seconds following activation in *ex vivo* preps from (I) ChAT$^+$ control and (J) ChAT$^+$ DREADD-administered mice
See also Figure S6 and Table S4

Table S1 - Extended GNPS Annotations of Metabolite Network Nodes (Related to Figure 3).
Extended annotations for networked (bold) MS/MS spectra from luminal cecal contents of activated TH^+ and $ChAT^+$ mice in Figures 3C and 3D, respectively.
Source Data Table S1
https://github.com/mazmanianlab/Griffiths_Yoo_et_al/blob/main/metabolomics/Table_S1-Extended_GNPS_annotations_of_Metabolite_Network_Notes_related_to_figure_3.xlsx

Table S2 - Gene Set Enrichment Analysis of Gene Ontology (GO) Terms (Related to Figure 5).
Gene set enrichment analysis of gene ontology (GO) terms that are upregulated in the distal SI and proximal colon of activated $ChAT^+$ and TH^+ mice.
Source Data Table S2
https://github.com/mazmanianlab/Griffiths_Yoo_et_al/blob/main/RNAseq/Table_S2-Gene_Set_Enrichment_Analysis_of_GO_related_to_figure_5.xlsx

Table S3 – Genes Related to T helper responses (Related to Figure 5).
List of genes in the transcriptomics dataset associated with T helper responses.
Source Data Table S3
https://github.com/mazmanianlab/Griffiths_Yoo_et_al/blob/main/RNAseq/Table_S3-Genes_Related_to_T_Helper_Responses.xlsx

Table S4 – Annotations of Colonic Migrating Motor Complexes (Related to Figure 6)
Video annotations of CMMCs in *ex vivo* colonic preparations from $ChAT^+$ and TH^+ mice at baseline and during activation.
Source Data Table S4
https://github.com/mazmanianlab/Griffiths_Yoo_et_al/blob/main/ex_vivo_motility/Table_S4%E2%80%93Annotations_of_Colonic_Migrating_Motor_Complexes_Related_to_figure_6.xlsx

Video S1 – Calcium Imaging of $ChAT^+$ activated Gut Neurons (Related to Figure S5)
Video of *in vivo* calcium imaging of GCaMP6f-expressing $ChAT^+$ activated neurons in the myenteric plexus at 5 Hz following C21 administration.
Source Data Video S1
https://github.com/mazmanianlab/Griffiths_Yoo_et_al/blob/main/ENS%20quantification/Video%20Supplement%201-%20GCaMP6F%20at%205Hz.avi

761 ## METHODS

762 **Mice**
763 All mouse experiments were performed in accordance with the NIH Guide for the Care and Use
764 of Laboratory Animals using protocols approved by the Institutional Animal Care and Use
765 Committee at the California Institute of Technology. Mice were fed ad libitum for the entire
766 duration of experiments. Homozygous TH-Cre (gift to V.G. from Ted Ebendal, B6.129X1-
767 Thtm1(cre)Te/Kieg (Lindeberg et al., 2004)) and ChAT-Cre (Jackson Laboratories, Bar Harbor,
768 ME- Stock# 028861, RRID:IMSR_JAX:028861) mice were bred to wild-type mice to yield the
769 male and female heterozygous Cre-mice used for our studies. Wild-type specific pathogen free
770 (SPF) C57BL/6 (Jackson Laboratories, Bar Harbor, ME- Stock #000664,
771 RRID:IMSR_JAX:000664) males and females were used for breeding and experiments.
772
773 **Virus Production**
774 Virus was produced using the methods described in Challis et al., 2019 and
775 dx.doi.org/10.17504/protocols.io.bzn6p5he. Briefly, human embryonic kidney (HEK293T) cells
776 were triple-transfected with pUCmini-iCAP-AAV-PHP.S, pHelper plasmid, and one of the
777 following pAAV genomes: CAG-NLS-GFP, hSYN1-tdTomato, GFAP-tdTomato, hSYN1-
778 mRuby2, hSYN1-DIO-mRuby2, hSYN1-mNeonGreen, hSYN1-DIO-mNeonGreen, hSYN1-
779 mTurquoise2, hSYN1-DIO-mTurquoise2, hSYN1-DIO-hM3Dq-mRuby2, CAG-GCaMP6f. Cells
780 were grown in DMEM + Glutamax + Pyruvate (Gibco, Gaithersburg, MD- Stock# 10569-010) +
781 5% FBS + non-essential amino acids (Gibco, Gaithersburg, MD- Stock# 11140-050) + penicillin-
782 streptomycin (Gibco, Gaithersburg, MD- Stock# 15070-063). Virus was precipitated from cells
783 and supernatant with an 8% PEG solution (wt/vol), and purified by ultracentrifugation using
784 15%, 25%, 40%, 60% stacked iodixanol gradients.
785
786 **Systemic Delivery of AAV**
787 Mice were anesthetized using 2% isoflurane. Virus was titered to $1x10^{12}$ vg, resuspended in a
788 volume of 100 µl with sterile PBS, and injected retro-orbitally as described in
789 dx.doi.org/10.17504/protocols.io.bzn6p5he.
790
791 **Neuronal activation of the GI tract**
792 See dx.doi.org/10.17504/protocols.io.bzp5p5q6. TH-Cre and ChAT-Cre mice were used for
793 these experiments. “Activated” mice were infected with AAV-PHP.S-hSYN1-DIO-hM3Dq-
794 mRuby2 and “Control Mice” were infected with AAV-PHP.S-hSYN1-DIO-mRuby2. This was to
795 control for both AAV-PHP.S-mediated expression and the effects of Compound 21
796 dihydrochloride (C21) (HelloBio, Princeton, NJ- HB6124). C21 was injected intraperitoneally
797 (i.p.) at a dose of 3 mg/kg for 10 consecutive days to both groups of mice. Mice for timecourse
798 experiments were single-housed in sterile cages with autoclaved water following the first C21
799 administration. Injections of C21 were administered at the same time every day (10AM). Mice
800 were sacrificed one hour after the day 10 injection.
801
802 **Tissue Preparation, Immunohistochemistry, Imaging, and Quantification**
803 Procedures are described in dx.doi.org/10.17504/protocols.io.bzp6p5re. 100 mg/kg of
804 pentobarbital (Euthasol - Virbac, Carros, France) was administered i.p., and tissues were
805 perfused with 30 mL of phosphate-buffered saline (PBS) and then cold 4% paraformaldehyde
806 (PFA) in PBS. GI tract was post-fixed in 4% PFA overnight at 4 ºC, and stored in PBS + 0.025%
807 sodium azide. Tissues that underwent subsequent immunohistochemistry were made
808 transparent by the passive CLARITY technique (PACT) (Treweek et al., 2015). Briefly, perfused
809 and fixed tissues were embedded with polymerized 4% (wt/vol) acrylamide, and lipids were
810 eliminated using 8% (wt/vol) SDS solution. Jugular-nodose ganglia and dorsal root ganglia

811 tissues were cryoprotected in 10% then 30% sucrose in PBS for 1 day each. Tissues were
812 embedded and flash frozen in OCT and cryostat sectioned into 40 µM sections. Spinal cord and
813 brain tissues were vibratome sectioned into 50 µM sections. Tissues were blocked in 3%
814 donkey serum and permeabilized with PBS + 0.3% Triton (PBST). Primary antibodies were
815 incubated in PBST for 48 hours and washed with PBST for 24 hours (replacing the wash
816 solution 3 times). Tissues were next incubated in secondary antibodies (and DAPI) for 24 hours
817 and washed in PBS for 48 hours, intermittently replacing the wash solution with fresh PBS.
818 Primary antibodies used were rabbit anti-PGP9.5 (1:300; Millipore Cat# AB1761-I,
819 RRID:AB_2868444), chicken anti-GFAP (1:500, BioLegend Cat# 829401, RRID:AB_2564929),
820 rabbit anti-tyrosine hydroxylase (1:500, Abcam Cat# ab112, RRID:AB_297840), rabbit anti-
821 choline acetyltransferase, (1:250, Abcam Cat# ab178850, RRID:AB_2721842), and mouse anti-
822 NeuN (1:300, Abcam Cat# ab104224, RRID:AB_10711040). Secondary antibodies used were
823 goat anti-chicken Alexa 647 (Thermo Fisher Scientific Cat# A32933TR, RRID:AB_2866500),
824 donkey anti-rabbit Alexa 568 (Thermo Fisher Scientific Cat# A10042, RRID:AB_2534017), goat
825 anti-rabbit Alexa 647 (Thermo Fisher Scientific Cat# A-21245 (also A21245),
826 RRID:AB_2535813), and goat anti-mouse Alexa 594 (Thermo Fisher Scientific Cat# A-11032,
827 RRID:AB_2534091). GI tissues imaged for virally-expressed, endogenous fluorescence were
828 made transparent using a sorbitol-based optical clearing method, Sca*l*eS (Hama et al., 2015).
829 Tissues were mounted in method-respective mounting media (RIMS and Scales S4) on a glass
830 slide with a 0.5mm spacer (iSpacer, SunJin Lab Co.). Images were acquired on Zeiss LSM 780
831 or 880, and microscope, laser settings, contrast, and gamma remained constant across images
832 that were directly compared. All confocal images were taken with the following objectives: Fluar
833 5× 0.25 M27 Plan-Apochromat, 10× 0.45 M27 (working distance 2.0 mm) and Plan-Apochromat
834 25× 0.8 Imm Corr DIC M27 multi-immersion. Neurons in each ganglion were counted by
835 counting cells that were of a distinct color. Colonic ganglia were defined as distinct if separated
836 by a width of 3 or more neurons.
837
838 **GCaMP6f Fluorescence in *Ex Vivo* Intestinal Preparations**
839 As described in dx.doi.org/10.17504/protocols.io.bzqap5se, small intestinal tissue was quickly
840 harvested from ChAT-Cre mice, flushed, and placed in oxygenated (95% O_2, 5% CO_2), ice cold
841 Krebs-Henseleit solution for 1 hour followed by 15 min at room temperature. A segment was cut
842 along the mesenteric attachment and pinned flat (mucosa facing down) on a Sylgard-lined
843 recording chamber (Warner Instruments, PH1) in oxygenated Krebs-Henseleit solution. C21
844 was added at 10nM and GCaMP6f fluorescence was detected on an upright microscope (Zeiss,
845 Oberkochen, Germany- Examiner D1).
846
847 **Metagenomics**
848 Procedures are described in dx.doi.org/10.17504/protocols.io.bzqep5te.
849 ***Fecal collection***
850 AAV-PHP.S-hSYN1-hM3Dq-mRuby2 (10^{12} vg) was delivered systemically to TH-Cre and ChAT-
851 Cre mice. 3-4 week after infection, C21 (3 mg/kg) was administered daily for 10 consecutive
852 days. Fecal pellets were collected in sterile containers one day before the initial C21 dose, and
853 on day 2, 6, and 10 of injections.
854 ***Fecal sample DNA extraction and library preparation***
855 DNA was extracted with the Qiagen MagAttract PowerSoil DNA kit as previously described
856 (Marotz et al., 2017).This protocol is optimized for an input quantity of 1 ng DNA per reaction.
857 Prior to library preparation, input DNA was transferred to a 384-well plate and quantified using a
858 PicoGreen fluorescence assay (ThermoFisher, Inc). Input DNA was then normalized to 1 ng in a
859 volume of 3.5 µL of molecular-grade water using an Echo 550 acoustic liquid-handling robot
860 (Labcyte, Inc). Enzyme mixes for fragmentation, end repair and A-tailing, ligation, and PCR
861 were prepared and added in approximately 1:8 scale volumes using a Mosquito HV

862 micropipetting robot (TTP Labtech). Fragmentation was performed at 37 °C for 20 min, followed
863 by end repair and A-tailing at 65 °C for 30 min.
864
865 Sequencing adapters and barcode indices were added in two steps, following the iTru adapter
866 protocol (Glenn et al., 2019). Universal "stub" adapter molecules and ligase mix were first added
867 to the end-repaired DNA using the Mosquito HV robot and ligation performed at 20 °C for 1 h.
868 Unligated adapters and adapter dimers were then removed using AMPure XP magnetic beads
869 and a BlueCat purification robot (BlueCat Bio). 7.5 µL magnetic bead solution was added to the
870 total adapter-ligated sample volume, washed twice with 70% EtOH, and then resuspended in
871 7 µL molecular-grade water.
872
873 Next, individual i7 and i5 were added to the adapter-ligated samples using the Echo 550 robot.
874 Because this liquid handler individually addresses wells, and we used the full set of 384 unique
875 error-correcting i7 and i5 indices, we were able to generate each plate of 384 libraries without
876 repeating any barcodes, eliminating the problem of sequence misassignment due to barcode
877 swapping (Costello et al., 2018; Sinha et al., 2017). To ensure that libraries generated on
878 different plates could be pooled if necessary, and to safeguard against the possibility of
879 contamination due to sample carryover between runs, we also iterated the assignment of i7 to i5
880 indices each run, such that each unique i7:i5 index combination was repeated only once every
881 147,456 libraries. 4.5 µL of eluted bead-washed ligated samples was added to 5.5 µL of PCR
882 master mix and PCR-amplified for 15 cycles. The amplified and indexed libraries were then
883 purified again using magnetic beads and the BlueCat robot, resuspended in 10 µL water, and
884 9 µL of final purified library transferred to a 384-well plate using the Mosquito HV liquid-handling
885 robot for library quantitation, sequencing, and storage. 384 samples were then normalized
886 based on a PicoGreen fluorescence assay.
887 ***Shallow shotgun metagenome sequencing and diversity analysis***
888 The Illumina data for each HiSeq lane was uploaded to Qiita, a tool with standardized pipelines
889 for processing and analyzing metagenomic data (Gonzalez et al., 2018). Adapter sequences
890 were removed from the reads using the Atropos v.1.1.15 (RRID:SCR_023962,
891 https://github.com/jdidion/atropos) (Didion et al., 2017) command (from the qp-shogun 0.1.5
892 pipeline) and the trimmed sequences were downloaded from Qiita. The reads for each sample
893 were filtered of any potential mouse contamination using Bowtie2 v.2-2.2.3
894 (RRID:SCR_016368, https://bowtie-bio.sourceforge.net/bowtie2/index.shtml) (Langmead and
895 Salzberg, 2012). The filtered reads were then aligned to the Web of Life (WoL) reference
896 phylogeny (Zhu et al., 2019) with Bowtie2 using an adapted SHOGUN pipeline (Hillmann et al.,
897 2018). The WoL contains 10,575 bacterial and archaeal genomes, with each genome
898 representing an operational taxonomic unit (OTU). Sequencing reads that did not map to a
899 single reference genome as well as reads that mapped to multiple genomes were not included
900 in the analysis. If an OTU had a relative abundance less than 0.01% in a given sample, the OTU
901 was not included for that sample. Additionally, OTUs with fewer than 5 assigned reads were not
902 considered. The samples were rarefied to a depth of 12,750 reads and those with fewer than
903 the rarefaction depth were excluded. The QIIME2 v.2019.7 (RRID:SCR_021258,
904 https://qiime2.org/) (Bolyen et al., 2019) DEICODE plugin was used to calculate the Aitchison
905 distances, a compositional beta diversity metric, and perform Robust Aitchison PCA to create
906 biplots that visualize relationships between features and samples (Martino et al., 2019). The
907 QIIME2 diversity plugin was used to calculate the other alpha- and beta-diversity metrics used
908 in this study.
909 ***Metagenomics-based functional profiling***
910 The filtered reads were also analyzed using HUMAnN2 v2.8.1 (RRID:SCR_016280,
911 https://huttenhower.sph.harvard.edu/humann2) (Franzosa et al., 2018) to establish functional
912 profiles for the samples. HUMAnN2 is a pipeline that begins by using MetaPhlAn 2 to compile

913 custom databases of reference genomes based on the species detected in a sample (Truong et
914 al., 2015). HUMAnN2 then maps the filtered reads onto these custom databases and the reads
915 that do not map to any of the references are then subjected to a translated search against
916 UniProt Reference Clusters or UniRef (RRID:SCR_010646, https://www.uniprot.org/help/uniref)
917 (Suzek et al., 2007). Here, the UniRef90 database was used for the translated search and
918 installed according to the HUMAnN2 documentation. The results from both the search
919 performed using the custom reference genome database and the search against the UniRef90
920 database were combined and the gene families identified in each sample were reported in units
921 of reads per kilobase (RPKs) to account for gene length. HUMAnN2 also compared the gene
922 families found in a sample with the MetaCyc pathways database (RRID:SCR_007778,
923 https://metacyc.org/) (Caspi et al., 2018) and output a table reporting the pathway abundances
924 found in each sample. After rarefying gene family tables to a depth of 166,000 RPKs and using
925 a depth of 22,600 for pathway abundances, the QIIME2 diversity and DEICODE plugins were
926 used to calculate alpha- and beta-diversity metrics. The metagenomics data from this study are
927 available from
928 (https://github.com/mazmanianlab/Griffiths_Yoo_et_al/tree/main/metagenomics).

929 **Metabolomics**
930 Procedures are described in dx.doi.org/10.17504/protocols.io.bzqfp5tn.
931 ***Sample preparation***
932 Frozen cecal samples were transported on dry ice for metabolomics analysis. The samples
933 were weighed and an extraction solvent (1:1 methanol to water with an internal standard of 1
934 µM sulfamethazine) was added at a 1:10 milligram to microliter ratio. The samples were then
935 homogenized using a TissueLyser II (Qiagen) for 5 minutes at 25 Hz followed by a 15 min
936 centrifugation at 14,000 rpm. 120 µL of supernatant was transferred to a 96-well DeepWell plate
937 (Eppendorf) and lyophilized using a CentriVap Benchtop Vacuum Concentrator (Labconco) and
938 stored at -80 ºC. At the time of data acquisition, the lyophilized plates were resuspended in a
939 1:1 methanol to water solvent spiked with 1 µM of sulfadimethoxine. The plates were vortexed
940 for 2 minutes, centrifuged at 14,000 rpm for 15 min and 120 µL of the supernatant was
941 transferred to a 96-well autosampler plate (Eppendorf). Plates were stored at 4 °C prior to
942 LCMS analysis.
943 ***Data acquisition***
944 The untargeted metabolomics analysis was completed using an ultra-high performance liquid
945 chromatography system (Thermo Dionex Ultimate 3000 UHPLC) coupled to an ultra-high
946 resolution quadrupole time of flight (qTOF) mass spectrometer (Bruker Daltonics MaXis HD). A
947 Phenomenex Kinetex column (C18 1.7 µm, 2.1 mm x 50 mm) was used for chromatographic
948 separation. An injection volume of 5 µL was used for each sample and a flow-rate of 0.500 mL
949 was used throughout the analysis. The mobile phase consisted of solvent A: 100% LC-MS
950 grade water spiked with 0.1% formic acid and solvent B: 100% LC-MS grade acetonitrile spiked
951 with 0.1% formic acid. The chromatographic gradient was as follows: 0.0–1.0 min, 5% B; 1.0–
952 9.0 min, 5–100% B; 9.0-11.0 min, 100% B; 11.0-11.5 min, 100-5% B; 11.5-12.5 min, 5% B. Data
953 was collected with electrospray ionization in positive mode, and was saved as .d file folders.
954 ***Data processing***
955 The raw .d data files were converted to mzXML format using Bruker Compass DataAnalysis 4.1
956 software. The resulting .mzXML file, the original .d file folders, and basic prep information sheet
957 are stored in the UC San Diego MassIVE data repository under the accession number
958 MSV000084550. For MS1 level feature detection, the open-source software MZmine version
959 2.51 (RRID:SCR_012040, https://mzmine.github.io/) was used. The parameters used are as
960 follows: 1) Mass Detection (Centroid, Noise Level MS1 1E3, MS2 1E2); 2) ADAP
961 Chromatogram Builder (Min Group size in # of scans=3, Group Intensity Threshold= 3E3, Min

962 Highest Intensity=1E3, m/z tolerance 0.01 m/z or 10.0 ppm); 3) Chromatogram Deconvolution
963 (Local Minimum Search>Chromatographic Threshold 0.01%, Minimum in RT range 0.50 min,
964 <Minimum Relative Height 0.01%, Minimum Absolute Height 3E3, Min Ratio of Peak Top/Edge
965 2, Peak Duration Range 0.05-0.50 min; m/z Calculation Auto, m/z range for MS2 pairing 0.01
966 Da, and RT Range for MS2 Pairing 0.1 min); Isotopic Peaks Grouper (m/z Tolerance 0.01 m/z
967 or 10.0 ppm, Retention Time Tolerance 0.3 min, Maximum Charge 4, Representative Ion Most
968 Intense); Join Aligner (m/z Tolerance 0.01 m/z or 10.0 ppm, Weight for m/z 75, Retention Time
969 Tolerance 0.3 min, Weight for RT 25); Gap-Filling Peak Finder (Intensity Tolerance 20%, m/z
970 Tolerance 0.005 m/z or 10.0 ppm, Retention Time Tolerance 0.2 min). The resulting feature
971 table was saved as a .csv file and .mgf file for use in GNPS and MetaboAnalyst.
972 ***Molecular networking and statistical analysis***
973 Molecular networking was performed using the feature networking tool available through the
974 Global Natural Products Social Molecular Networking (GNPS, RRID:SCR_019012,
975 https://gnps.ucsd.edu/ProteoSAFe/static/gnps-splash.jsp) portal:
976 https://gnps.ucsd.edu/ProteoSAFe/index.jsp?params=%7B%22workflow%22:%22FEATURE-
977 BASED-MOLECULAR-
978 NETWORKING%22,%22library_on_server%22:%22d.speclibs;%22%7D.
979 The annotations obtained using this workflow fall under MSI level 2 or 3 and were used for
980 feature analysis (Sumner et al., 2007). Briefly, level 2 compounds are putatively annotated,
981 meaning they are not identified using chemical reference standards but rather based on
982 physical properties and/or spectral similarities to available spectral libraries (publicly available
983 and purchased NIST17 CID). Level 3 compounds are putatively characterized classes of
984 compounds identified similarly to level 2 compounds. The feature-based molecular networking
985 workflow on GNPS (Nothias et al., 2019) was utilized in order to analyze the spectra associated
986 with the feature tables produced using the open source software Mzmine version 2.51
987 (RRID:SCR_012040, https://mzmine.github.io/) (Pluskal et al., 2010). The .mgf and .csv outputs
988 from MZmine v2.51 were used to run the workflow. The GNPS workflow parameters used were
989 as follows: Precursor Ion Mass 0.02 Da, Fragment Ion Mass Tolerance 0.02 Da, Min Pairs Cos
990 0.7, Minimum Matched Fragments 6, Maximum Shift Between Precursors 500 Da, Network
991 TopK 10, Maximum Connected Component Size (Beta) 100, and the files were row sum
992 normalized. Default parameters were used for the rest of the settings. Visualizations and
993 statistical analyses were performed using QIIME 2 v.2019.10 (RRID:SCR_021258) (Bolyen et
994 al., 2019), MetaboAnalyst (RRID:SCR_015539, https://www.metaboanalyst.ca/) and Cytoscape
995 v3.7.2 (RRID:SCR_003032, https://cytoscape.org/). The metabolomics data from this study are
996 available from
997 (https://github.com/mazmanianlab/Griffiths_Yoo_et_al/tree/main/metabolomics).
998
999 **Proteome Preparation**
1000 Procedures are described in dx.doi.org/10.17504/protocols.io.bzqcp5sw.
1001 ***Protein extraction***
1002 Mice were sacrificed 1 hour after the final C21 administration and cecal contents were isolated
1003 and resuspended in 400 μl of phosphate buffered solution and centrifuged at 20,000 xg to spin
1004 down cells and lysate. Protein was isolated from the resulting supernatant using Wessel-
1005 Flügge's methanol/chloroform extraction method (Wessel and Flügge, 1984). Briefly, MeOH and
1006 chloroform were added to the samples at a 4:1 and 1:1 ratio, respectively. Next, dH_2O was
1007 added at a 3:1 ratio, samples were vortexed and centrifuged at 20,000 xg. Resulting
1008 precipitated protein was collected and washed with MeOH. Precipitated protein was centrifuged
1009 and left to air dry, and stored at -20 ºC until protein digestion.
1010 ***In-solution protein digestion and desalting***
1011 Precipitated protein samples were denatured in 40 µL of 8M Urea (100 mM Tris-HCl pH 8.5). To
1012 reduce disulfide bonds, 1.25 µL of 100 mM Tris(2-carboxyethyl)Phosphine was added and

1013 incubated at room temperature (RT) for 20 minutes. Then 1.8 µL of 250 mM iodoacetamide was
1014 added and incubated at RT in the dark to alkylate cysteines. The first step of digestion was
1015 initiated by adding 1 µL of 0.1 µg/µL of lysyl endopeptidase. After 4 hours of incubation, the urea
1016 concentration was adjusted to 2 M by adding 120 µL of 100 mM Tris-HCl pH 8.5. The second
1017 step of digestion was done by adding 2.5 µL of 2µg/µL trypsin plus 1.6 µL of 100 mM $CaCl_2$ and
1018 incubating overnight in the dark. Formic acid was added to stop trypsin digestion. Digested
1019 peptides were desalted by HPLC using a C8 peptide microtrap (Microm Bioresources),
1020 lyophilized, and diluted to 200 ng/µl in 0.2% formic acid prior to LC-MS/MS analysis.
1021 ***LC-MS/MS***
1022 Samples were analyzed on a Q Exactive HF Orbitrap mass spectrometer coupled to an EASY
1023 nLC 1200 liquid chromatographic system (Thermo Scientific, San Jose, CA). Approximately 200
1024 ng of peptides were loaded on a 50 µm I.D. × 25 cm column with a 10 µm electrospray tip
1025 (PicoFrit from New Objective, Woburn, MA) in-house-packed with ReproSil-Pur C18-AQ 1.9 µm
1026 (Dr. Maisch, Ammerbuch, Germany). Solvent A consisted of 2% MeCN in 0.2% FA and solvent
1027 B consisted of 80% MeCN in 0.2% FA. A non-linear 60 minute gradient from 2% B to 40% B
1028 was used to separate the peptides for analysis. The mass spectrometer was operated in a data-
1029 dependent mode, with MS1 scans collected from 400-1650 m/z at 60,000 resolution and MS/MS
1030 scans collected from 200-2000 m/z at 30,000 resolution. Dynamic exclusion of 45 s was used.
1031 The top 12 most abundant peptides with charge states between 2 and 5 were selected for
1032 fragmentation with normalized collision energy of 28.
1033 ***Peptide and protein identification***
1034 Thermo .raw files were converted to .ms1 and .ms2 files using RawConverter 1.1.0.18 (He et
1035 al., 2015) operating in data dependent mode and selecting for monoisotopic m/z. Tandem mass
1036 spectra (.ms2 files) were identified by a database search method using the Integrated
1037 Proteomics Pipeline 6.5.4 (IP2, Integrated Proteomics Applications, Inc.,
1038 http://www.integratedproteomics.com). Briefly, databases containing forward and reverse
1039 (decoy) (Elias and Gygi, 2007; Peng et al., 2003) peptide sequences were generated from *in*
1040 *silico* trypsin digestion of either the mouse proteome (UniProt; Oct. 2, 2019) or protein
1041 sequences derived from large comprehensive public repositories (ComPIL 2.0) (Park et al.,
1042 2018). Tandem mass spectra were matched to peptide sequences using the
1043 ProLuCID/SEQUEST (1.4) (Xu et al., 2015; 2006) software package. The validity of spectrum-
1044 peptide matches was assessed using the SEQUEST-defined parameters XCorr (cross-
1045 correlation score) and DeltaCN (normalized difference in cross-correlation scores) in the
1046 DTASelect2 (2.1.4) (Cociorva et al., 2007; Tabb et al., 2002) software package. Search settings
1047 were configured as follows: (1) 5 ppm precursor ion mass tolerance, (2) 10 ppm fragment ion
1048 mass tolerance, (3) 1% peptide false discovery rate, (4) 2 peptide per protein minimum, (5) 600-
1049 6000 Da precursor mass window, (6) 2 differential modifications per peptide maximum
1050 (methionine oxidation: M+15.994915 Da), (7) unlimited static modifications per peptide (cysteine
1051 carbamidomethylation: C+57.02146 Da), and (8) the search space included half- and fully-
1052 tryptic (cleavage C-terminal to K and R residues) peptide candidates with unlimited (mouse
1053 database, custom metagenomic shotgun database) or 2 missed cleavage events (ComPIL 2.0).
1054 ***Differential analysis of detected proteins using peptide-spectrum matches (spectral***
1055 ***counts)***
1056 Detected proteins were grouped by sequence similarity into "clusters" using CD-HIT 4.8.1
1057 (RRID:SCR_007105, http://weizhong-lab.ucsd.edu/cd-hit/) (Fu et al., 2012; Li and Godzik, 2006;
1058 Li et al., 2001) at the following similarity cut-offs: 65%, 75%, 85%, and 95%. The following is an
1059 example command line input: "cd-hit -i fastafile.fasta -o outputfile -c 0.65 -g 1 -d 0". Tandem
1060 mass spectra identified as peptides (peptide spectrum matches, PSMs) were mapped to CD-
1061 HIT generated clusters. PSMs mapping to >1 cluster were discarded. Cluster-PSM tables were
1062 generated and differential analysis was performed in DESeq2 (1.25.13, RRID:SCR_015687,
1063 https://bioconductor.org/packages/release/bioc/html/DESeq2.html) (Love et al., 2014). Briefly,

count data (PSMs) were modeled using the negative binomial distribution, and the mean-variance relationship was estimated. Variance was estimated using an information sharing approach whereby a single feature's (or cluster's) variance was estimated by taking into account variances of other clusters measured in the same experiment. Feature significance calling and ranking were performed using estimated effect sizes. Multiple testing correction was performed by the Benjamini-Hochberg method within the DESeq2 package. Volcano plots were generated in Prism (GraphPad).

Differential analysis of detected proteins using ion intensity (precursor intensity)

Detected proteins were grouped into "clusters" by sequence similarity using CD-HIT 4.8.1 (Fu et al., 2012; Li and Godzik, 2006; Li et al., 2001) at the following similarity cut-offs: 65%, 75%, 85%, and 95%. The following is an example command line input: "cd-hit -i fastafile.fasta -o outputfile -c 0.65 -g 1 -d 0". Using the Census software package (Park et al.; 2008) (Integrated Proteomics Pipeline 6.5.4), peptide ion intensities were calculated from .ms1 files. Peptide ion intensities were assigned to their parent peptide, then parent peptides were mapped to their appropriate CD-HIT generated clusters. Ion intensities belonging to parent peptides that mapped to >1 CD-HIT cluster were discarded. Cluster-ion intensity tables were generated.

Ion intensity data were analyzed using the Differential Enrichment analysis of Proteomics data DEP package (RRID:SCR_023090, https://bioconductor.org/packages/release/bioc/html/DEP.html) (Zhang et al., 2018) operating in R. Intensity values were automatically Log2 transformed in DEP. The cluster list was subsequently filtered with the 'filter_proteins' function such that clusters with missing values above a 65% threshold were discarded. Remaining intensities were further transformed by the 'normalize_vsn' function (Huber et al., 2002). Missing data in remaining clusters were imputed using a mixed approach. Clusters where either the control or treatment group contained only null entries were classified as 'missing not at random' (MNAR) and imputed with 0 values. All other groups were treated as 'missing at random' (MAR) and imputed using the maximum likelihood method ('MLE') (Gatto and Lilley, 2012). Note that for a given cluster, missing values for treatment groups were imputed separately by treatment group. Differential expression analyses were performed on filled-in cluster-ion intensity tables using the 'test_diff' function (Ritchie et al., 2015) and multiple testing correction was performed using the 'add_rejections' function.

Network analysis using the STRING database

Upregulated proteins with a nominal p-value < 0.2 were searched against protein-protein interactions in the STRING database (RRID:SCR_005223, http://www.string-db.org) where high confidence interactions are selected for. Briefly, the STRING database sources protein-protein interactions from primary databases consisting of genomic context predictions, high-throughput lab experiments, (conserved) co-expression, automated text mining, and previous knowledge in databases (Szklarczyk et al., 2019).

Metaproteome analysis using Unipept

Upregulated tryptic, microbial peptide sequences, with fold change and nominal p-value cutoffs of >2 and <0.2, respectively, were input into Unipept (http://unipept.ugent.be) (Gurdeep Singh et al., 2019; Mesuere et al., 2015), equating leucine and isoleucine and filtering duplicate peptides. Briefly, Unipept indexes tryptic peptide sequences from the UniProtKB and details peptides with NCBI's taxonomic database. Lowest common ancestor was calculated for each tryptic peptide. The proteomics data from this study are available from (https://github.com/mazmanianlab/Griffiths_Yoo_et_al/tree/main/proteomics).

3' mRNA sequencing

Procedures are described in dx.doi.org/10.17504/protocols.io.bzqbp5sn.

Tissue collection and RNA extraction

1115 Mice were cervically dislocated and the GI tract was removed. 1 cm of tissue above and below
1116 the cecum were dissected and cleaned to represent tissue from the distal SI and proximal colon,
1117 respectively. Tissue was homogenized in TRIzol (ThermoFisher Scientific, Waltham. MA- Cat.
1118 No. 15596018) solution using a bead-based homogenizing method, and total RNA was
1119 extracted using chloroform per manufacturer's instructions.
1120 ***Library preparation, sequencing, and analysis***
1121 The cDNA libraries were prepared using the QuantSeq 3'mRNA-Seq Library Prep Kit FWD for
1122 Illumina (Lexogen, Greenland, NH) supplemented with UMI (unique molecular index) as per the
1123 manufacturer's instructions. Briefly, total RNA was reverse transcribed using oligo (dT) primers.
1124 The second cDNA strand was synthesized by random priming, in a manner such that DNA
1125 polymerase is efficiently stopped when reaching the next hybridized random primer, so only the
1126 fragment closest to the 3' end gets captured for later indexed adapter ligation and PCR
1127 amplification. UMIs were incorporated to the first 6 bases of each read, followed by 4 bases of
1128 spacer sequences. UMIs are used to eliminate possible PCR duplicates in sequencing datasets
1129 and therefore facilitate unbiased gene expression profiling. The basic principle behind the UMI
1130 deduplication step is to collapse reads with identical mapping coordinates and UMI sequences.
1131 This step helps increase the accuracy of sequencing read counts for downstream analysis of
1132 gene expression levels. The processed libraries were assessed for size distribution and
1133 concentration using the Bioanalyzer High Sensitivity DNA Kit (Agilent Technologies, Santa
1134 Clara, CA- Cat. No. 5067-4626 and -4627). Pooled libraries were diluted to 2 nM in EB buffer
1135 (Qiagen, Hilden, Germany, Cat. No. 19086) and then denatured using the Illumina protocol. The
1136 libraries were pooled and diluted to 2 nM using 10 mM Tris-HCl, pH 8.5 and then denatured
1137 using the Illumina protocol. The denatured libraries were diluted to 10 pM with pre-chilled
1138 hybridization buffer and loaded onto an Illumina MiSeq v3 flow cell for 150 cycles using a single-
1139 read recipe according to the manufacturer's instructions. Single-end 75 bp reads (max 4.5M
1140 reads) were obtained. De-multiplexed sequencing reads were generated using Illumina
1141 BaseSpace.
1142
1143 UMI specific workflows that were developed and distributed by Lexogen were used to extract
1144 reads that are free from PCR artifacts (i.e., deduplication). First, the umi2index tool was used to
1145 add the 6 nucleotide UMI sequence to the identifier of each read and trim the UMI from the start
1146 of each read. This generated a new FASTQ file, which was then processed through trimming
1147 and alignment. Second, after the quality and polyA trimming by BBDuk (Bestus Bioinformaticus
1148 Duk, RRID:SCR_016969, https://jgi.doe.gov/data-and-tools/bbtools/bb-tools-user-guide/bbduk-
1149 guide/) and alignment by HISAT2 (version 2.1.0, RRID:SCR_015530,
1150 https://daehwankimlab.github.io/hisat2/) (Kim et al., 2015), the mapped reads were collapsed
1151 according to the UMI sequence of each read. Reads were collapsed if they had the same
1152 mapping coordinates (CIGAR string) and identical UMI sequences. Collapsing reads in this
1153 manner removes PCR duplicates. Read counts were calculated using HTSeq
1154 (RRID:SCR_005514, https://htseq.readthedocs.io/en/release_0.9.1/) (Anders et al., 2015) by
1155 supplementing Ensembl gene annotation (GRCm38.78). Raw read counts were run through
1156 ShinySeq to obtain differentially expressed genes and downstream gene ontology analyses
1157 (Sundararajan et al., 2019). The RNAseq data from this study are available from
1158 (https://github.com/mazmanianlab/Griffiths_Yoo_et_al/tree/main/RNAseq).
1159
1160 **Whole Gut Transit Time, Fecal Water Content, and Fecal Output**
1161 Procedures are described in dx.doi.org/10.17504/protocols.io.36wgq3p1xlk5/v1.
1162 6% (w/v) carmine red (Sigma-Aldrich, St. Louis, MO) with 0.5% methylcellulose (Sigma-Aldrich)
1163 was dissolved and autoclaved prior to use. ChAT-Cre and TH-Cre mice were administered C21
1164 (3 mg/kg) intraperitoneally, and subsequently orally gavaged with 150 µL of carmine red
1165 solution. Mice were single-housed with no bedding for the duration of the experiment, and

1166 animals were not fasted beforehand. Over the 5 hours following gavage, the time of expulsion
1167 was recorded for each fecal pellet, and each pellet was collected in pre-weighed, 1.5 mL
1168 microcentrifuge tube. Each pellet collected was checked for the presence of carmine red, and
1169 the time of initial carmine red pellet expulsion was recorded as GI transit time. The mass of
1170 collected fecal pellets was determined, and pellets were left to dry in an 80 ºC oven for 2 days
1171 before weighing the desiccated pellets and calculating the pellets' initial water content. Fecal
1172 output rate for each mouse was calculated as the total number of pellets expelled during the 5
1173 hour time course post-C21 administration divided by the time the last fecal pellet was expelled.
1174
1175 **Colonic Migrating Motor Complexes in *Ex Vivo* Intestinal Preparations**
1176 Procedures are described in dx.doi.org/10.17504/protocols.io.n92ldm61nl5b/v1.
1177 Intact colons were dissected from cervically-dislocated ChAT-Cre and TH-Cre mice, flushed and
1178 placed in pre-oxygenated (95% O_2, 5% CO_2) Krebs-Henseleit solution at RT. Proximal and
1179 distal ends were cannulated to 2 mm diameter tubes and secured in the center of an organ bath
1180 with continuously oxygenated Krebs-Henseleit solution at 37 ºC. Syringe pumps were
1181 connected to the inlet and outlet tubes to maintain a flow of solution at a rate of 500 µL/min
1182 through the colon. The system was allowed to equilibrate for 30 minutes before recording.
1183 Baseline recordings were taken for 30 minutes, then the Krebs solution in the organ bath was
1184 briefly removed, mixed with C21 to a final concentration of 2 µM, and replaced in the organ
1185 bath. Recordings were taken for another 30 minutes.
1186

1187 **REFERENCES**

1188 Alavi, S., Mitchell, J.D., Cho, J.Y., Liu, R., Macbeth, J.C., and Hsiao, A. (2020). Interpersonal
1189 Gut Microbiome Variation Drives Susceptibility and Resistance to Cholera Infection. Cell *181*,
1190 1533–1546.e13.

1191 Albenberg, L.G., and Wu, G.D. (2014). Diet and the intestinal microbiome: associations,
1192 functions, and implications for health and disease. Gastroenterology *146*, 1564–1572.

1193 Anders, S., Pyl, P.T., and Huber, W. (2015). HTSeq--a Python framework to work with high-
1194 throughput sequencing data. Bioinformatics *31*, 166–169.

1195 Anlauf, M., Schäfer, M.K.H., Eiden, L., and Weihe, E. (2003). Chemical coding of the human
1196 gastrointestinal nervous system: cholinergic, VIPergic, and catecholaminergic phenotypes. The
1197 Journal of Comparative Neurology *459*, 90–111.

1198 Aries, V., Crowther, J.S., Drasar, B.S., and Hill, M.J. (1969). Degradation of bile salts by human
1199 intestinal bacteria. Gut *10*, 575–576.

1200 Bahrami, S., and Drabløs, F. (2016). Gene regulation in the immediate-early response process.
1201 Advances in Biological Regulation *62*, 37–49.

1202 Baumuratov, A. S., Antony, P. M. A., Ostaszewski, M., He, F., Salamanca, L., Antunes, L.,
1203 Weber, J., Longhino, L., Derkinderen, P., Koopman, W. J. H., Diederich, N. J. (2016). Enteric
1204 neurons from Parkinson's disease patients display ex vivo aberrations in mitochondrial
1205 structure. Scientific Reports *6*.

1206 Begley, M., Sleator, R.D., Gahan, C.G.M., and Hill, C. (2005). Contribution of three bile-
1207 associated loci, bsh, pva, and btlB, to gastrointestinal persistence and bile tolerance of Listeria
1208 monocytogenes. Infect. Immun. *73*, 894–904.

1209 Benskey, M.J., Kuhn, N.C., Galligan, J.J., Garcia, J., Boye, S.E., Hauswirth, W.W., Mueller, C.,
1210 Boye, S.L., and Manfredsson, F.P. (2015). Targeted gene delivery to the enteric nervous
1211 system using AAV: a comparison across serotypes and capsid mutants. Mol. Ther. *23*, 488–
1212 500.

1213 Bhavsar, A.S., Verma, S., Lamba, R., Lall, C.G., Koenigsknecht, V., and Rajesh, A. (2013).
1214 Abdominal manifestations of neurologic disorders. Radiographics *33*, 135–153.

1215 Bolyen, E., Rideout, J.R., Dillon, M.R., Bokulich, N.A., Abnet, C.C., Al-Ghalith, G.A., Alexander,
1216 H., Alm, E.J., Arumugam, M., Asnicar, F., et al. (2019). Reproducible, interactive, scalable and
1217 extensible microbiome data science using QIIME 2. Nat Biotechnol *37*, 852–857.

1218 Bravo, J.A., Forsythe, P., Chew, M.V., Escaravage, E., Savignac, H.M., Dinan, T.G.,
1219 Bienenstock, J., and Cryan, J.F. (2011). Ingestion of Lactobacillus strain regulates emotional
1220 behavior and central GABA receptor expression in a mouse via the vagus nerve. Proceedings of
1221 the National Academy of Sciences *108*, 16050–16055.

1222 Browning, K.N. and Travagli R.A. (2014). Central nervous system control of gastrointestinal
1223 motility and secretion and modulation of gastrointestinal functions. Compr Physiol. *4*, 1339-68.

1224 Bruel-Jungerman, E., Davis, S., and Laroche, S. (2016). Brain Plasticity Mechanisms and
1225 Memory: A Party of Four. Neuroscientist *13*, 492–505.

1226 Carabotti, M., Scirocco, A., Maselli, M.A., and Severi, C. (2015). The gut-brain axis: interactions
1227 between enteric microbiota, central and enteric nervous systems. Ann Gastroenterol *28*, 203–
1228 209.

1229 Carroll, I.M., Ringel-Kulka, T., Ferrier, L., Wu, M.C., Siddle, J.P., Bueno, L., and Ringel, Y.
1230 (2013). Fecal protease activity is associated with compositional alterations in the intestinal
1231 microbiota. PloS One *8*, e78017.

1232 Caspi, R., Billington, R., Fulcher, C.A., Keseler, I.M., Kothari, A., Krummenacker, M.,
1233 Latendresse, M., Midford, P.E., Ong, Q., Ong, W.K., et al. (2018). The MetaCyc database of
1234 metabolic pathways and enzymes. Nucleic Acids Res *46*, D633–D639.

1235 Cekanaviciute, E., Yoo, B.B., Runia, T.F., Debelius, J.W., Singh, S., Nelson, C.A., Kanner, R.,
1236 Bencosme, Y., Lee, Y.K., Hauser, S.L., et al. (2017). Gut bacteria from multiple sclerosis
1237 patients modulate human T cells and exacerbate symptoms in mouse models. Proc. Natl. Acad.
1238 Sci. U.S.a. *114*, 10713–10718.

1239 Cersosimo, M.G., Raina, G.B., Pecci, C., Pellene, A., Calandra, C.R., Gutiérrez, C., Micheli,
1240 F.E., and Benarroch, E.E. (2013). Gastrointestinal manifestations in Parkinson's disease:
1241 prevalence and occurrence before motor symptoms. J. Neurol. *260*, 1332–1338.

1242 Challis, R.C., Ravindra Kumar, S., Chan, K.Y., Challis, C., Beadle, K., Jang, M.J., Kim, H.M.,
1243 Rajendran, P.S., Tompkins, J.D., Shivkumar, K., et al. (2019). Systemic AAV vectors for
1244 widespread and targeted gene delivery in rodents. Nature Protocols *14*, 379–414.

1245 Chan, K.Y., Jang, M.J., Yoo, B.B., Greenbaum, A., Ravi, N., Wu, W.-L., Sánchez-Guardado, L.,
1246 Lois, C., Mazmanian, S.K., Deverman, B.E., et al. (2017). Engineered AAVs for efficient
1247 noninvasive gene delivery to the central and peripheral nervous systems. Nat. Neurosci. *20*,
1248 1172–1179.

1249 Chen, T.-W., Wardill, T.J., Sun, Y., Pulver, S.R., Renninger, S.L., Baohan, A., Schreiter, E.R.,
1250 Kerr, R.A., Orger, M.B., Jayaraman, V., et al. (2013). Ultrasensitive fluorescent proteins for
1251 imaging neuronal activity. Nature *499*, 295–300.

1252 Cociorva, D., L Tabb, D., and Yates, J.R. (2007). Validation of Tandem Mass Spectrometry
1253 Database Search Results Using DTASelect. Current Protocols in Bioinformatics *16*.

1254 Costello, M., Fleharty, M., Abreu, J., Farjoun, Y., Ferriera, S., Holmes, L., Granger, B., Green,
1255 L., Howd, T., Mason, T., et al. (2018). Characterization and remediation of sample index swaps
1256 by non-redundant dual indexing on massively parallel sequencing platforms. BMC Genomics
1257 *19*, 332–10.

1258 de Aguiar Vallim, T.Q., Tarling, E.J., and Edwards, P.A. (2013). Pleiotropic roles of bile acids in
1259 metabolism. Cell Metabolism *17*, 657–669.

1260 Del Giudice, E., Staiano, A., Capano, G., Romano, A., Florimonte, L., Miele, E., Ciarla, C.,
1261 Campanozzi, A., and Crisanti, A.F. (1999). Gastrointestinal manifestations in children with
1262 cerebral palsy. Brain Dev. *21*, 307–311.

1263 Delpino, M.V., Marchesini, M.I., Estein, S.M., Comerci, D.J., Cassataro, J., Fossati, C.A., and
1264 Baldi, P.C. (2007). A bile salt hydrolase of Brucella abortus contributes to the establishment of a
1265 successful infection through the oral route in mice. Infect. Immun. *75*, 299–305.

1266 Deneux, T., Kaszas, A., Szalay, G., Katona, G., Lakner, T., Grinvald, A., Rózsa, B., and
1267 Vanzetta, I. (2016). Accurate spike estimation from noisy calcium signals for ultrafast three-
1268 dimensional imaging of large neuronal populations in vivo. Nature Communications *7*, 12190–
1269 17.

1270 Derrien, M., Vaughan, E.E., Plugge, C.M., and de Vos, W.M. (2004). Akkermansia muciniphila
1271 gen. nov., sp. nov., a human intestinal mucin-degrading bacterium. International Journal of
1272 Systematic and Evolutionary Microbiology *54*, 1469–1476.

1273 Deverman, B.E., Pravdo, P.L., Simpson, B.P., Kumar, S.R., Chan, K.Y., Banerjee, A., Wu, W.-
1274 L., Yang, B., Huber, N., Pasca, S.P., et al. (2016). Cre-dependent selection yields AAV variants
1275 for widespread gene transfer to the adult brain. Nat Biotechnol *34*, 204–209.

1276 Didion, J.P., Martin, M., and Collins, F.S. (2017). Atropos: specific, sensitive, and speedy
1277 trimming of sequencing reads. PeerJ *5*, e3720.

1278 Donaldson, G.P., Ladinsky, M.S., Yu, K.B., Sanders, J.G., Yoo, B.B., Chou, W.C., Conner,
1279 M.E., Earl, A.M., Knight, R., Bjorkman, P.J., et al. (2018). Gut microbiota utilize immunoglobulin
1280 A for mucosal colonization. Science *360*, 795–800.

1281 Donaldson, G.P., Lee, S.M., and Mazmanian, S.K. (2015). Gut biogeography of the bacterial
1282 microbiota. Nat Rev Micro *14*, 20–32.

1283 Donowitz, M., Singh, S., Salahuddin, F.F., Hogema, B.M., Chen, Y., Gucek, M., Cole, R.N.,
1284 Ham, A., Zachos, N.C., Kovbasnjuk, O., et al. (2007). Proteome of murine jejunal brush border
1285 membrane vesicles. J. Proteome Res. *6*, 4068–4079.

1286 Drokhlyansky, E., Smillie, C.S., Van Wittenberghe, N., Ericsson, M., Griffin, G.K., Eraslan, G.,
1287 Dionne, D., Cuoco, M.S., Goder-Reiser, M.N., Sharova, T., et al. (2020). The Human and
1288 Mouse Enteric Nervous System at Single-Cell Resolution. Cell *182*, 1606–1622.e1623.

1289 Elias, J.E., and Gygi, S.P. (2007). Target-decoy search strategy for increased confidence in
1290 large-scale protein identifications by mass spectrometry. Nat. Methods *4*, 207–214.

1291 Everard, A., Belzer, C., Geurts, L., Ouwerkerk, J.P., Druart, C., Bindels, L.B., Guiot, Y., Derrien,
1292 M., Muccioli, G.G., Delzenne, N.M., et al. (2013). Cross-talk between Akkermansia muciniphila
1293 and intestinal epithelium controls diet-induced obesity. Proc. Natl. Acad. Sci. U.S.a. *110*, 9066–
1294 9071.

1295 Finneran, D.J., Njoku, I.P., Flores-Pazarin, D., Ranabothu, M. R., Nash, K.R., Morgan, D., and
1296 Gordon, M.N. (2021). Towards Development of Neuron Specific Transduction After Systemic
1297 Delivery of Viral Vectors. Frontiers in Neurology *12*, 685802.

1298 Fiorucci, S., Biagioli, M., Zampella, A., and Distrutti, E. (2018). Bile Acids Activated Receptors
1299 Regulate Innate Immunity. Frontiers in Immunology *9*, eaao1605–eaao1617.

1300 Flandez, M., Guilmeau, S., Blache, P., and Augenlicht, L.H. (2008). KLF4 regulation in intestinal
1301 epithelial cell maturation. Experimental Cell Research *314*, 3712–3723.

1302 Foong, J.P.P., Tough, I.R., Cox, H.M., and Bornstein, J.C. (2014). Properties of cholinergic and
1303 non-cholinergic submucosal neurons along the mouse colon. The Journal of Physiology *592*,
1304 777–793.

1305 Franzosa, E.A., McIver, L.J., Rahnavard, G., Thompson, L.R., Schirmer, M., Weingart, G.,
1306 Lipson, K.S., Knight, R., Caporaso, J.G., Segata, N., et al. (2018). Species-level functional
1307 profiling of metagenomes and metatranscriptomes. Nat. Methods *15*, 962–968.

1308 Fried, D.E., and Gulbransen, B.D. (2015). In situ Ca2+ imaging of the enteric nervous system.
1309 JoVE.

1310 Fu, L., Niu, B., Zhu, Z., Wu, S., and Li, W. (2012). CD-HIT: accelerated for clustering the next-
1311 generation sequencing data. Bioinformatics *28*, 3150–3152.

1312 Fung, C., Koussoulas, K., Unterweger, P., Allen, A. M., Bornstein, J. C., Foong, J. P. P. (2018).
1313 Cholinergic Submucosal Neurons Display Increased Excitability Following in Vivo Cholera Toxin
1314 Exposure in Mouse Ileum. Sec. Gastrointestinal Sciences 9.

1315 Furness, J.B. (2012). The enteric nervous system and neurogastroenterology. Nature Reviews
1316 Gastroenterology and Hepatology *9*, 286–294.

1317 Furness, J.B., Callaghan, B.P., Rivera, L.R., and Cho, H.-J. (2014). The Enteric Nervous
1318 System and Gastrointestinal Innervation: Integrated Local and Central Control. In The Enteric
1319 Nervous System, (New York, NY: Springer New York), pp. 39–71.

1320 Furness, J.B. (2006). The Enteric Nervous System (Wiley-Blackwell).

1321 Gabanyi, I., Muller, P.A., Feighery, L., Oliveira, T.Y., Costa-Pinto, F.A., and Mucida, D. (2016).
1322 Neuro-immune Interactions Drive Tissue Programming in Intestinal Macrophages. Cell *164*,
1323 378–391.

1324 Gatto, L., and Lilley, K.S. (2012). MSnbase-an R/Bioconductor package for isobaric tagged
1325 mass spectrometry data visualization, processing and quantitation. Bioinformatics *28*, 288–289.

1326 Gershon, M.D. (2015). The Enteric Nervous System: A Second Brain. Hospital Practice *34*, 31–
1327 52.

1328 Glenn, T.C., Nilsen, R.A., Kieran, T.J., Sanders, J.G., Bayona-Vásquez, N.J., Finger, J.W.,
1329 Pierson, T.W., Bentley, K.E., Hoffberg, S.L., Louha, S., et al. (2019). Adapterama I: universal
1330 stubs and primers for 384 unique dual-indexed or 147,456 combinatorially-indexed Illumina
1331 libraries (iTru & iNext). PeerJ *7*, e7755.

1332 Gonzalez, A., Navas-Molina, J.A., Kosciolek, T., McDonald, D., Vázquez-Baeza, Y.,
1333 Ackermann, G., DeReus, J., Janssen, S., Swafford, A.D., Orchanian, S.B., et al. (2018). Qiita:
1334 rapid, web-enabled microbiome meta-analysis. Nat. Methods *15*, 796–798.

1335 Gottlieb, A., and Canbay, A. (2019). Why Bile Acids Are So Important in Non-Alcoholic Fatty
1336 Liver Disease (NAFLD) Progression. Cells *8*.

1337 Grundy, D., and Brookes, S. (2011). Neural Control of Gastrointestinal Function. Colloquium
1338 Series on Integrated Systems Physiology: From Molecule to Function *3*, 1–134.

1339 Gurdeep Singh, R., Tanca, A., Palomba, A., Van der Jeugt, F., Verschaffelt, P., Uzzau, S.,
1340 Martens, L., Dawyndt, P., and Mesuere, B. (2019). Unipept 4.0: Functional Analysis of
1341 Metaproteome Data. J. Proteome Res. *18*, 606–615.

1342 Haenraets, K., Foster, E., Johannssen, H., Kandra, V., Frezel, N., Steffen, T., Jaramillo, V.,
1343 Paterna, J.-C., Zeilhofer, H.U., and Wildner, H. (2017). Spinal nociceptive circuit analysis with
1344 recombinant adeno-associated viruses: the impact of serotypes and promoters. Journal of
1345 Neurochemistry *142*, 721–733.

1346 Hama, H., Hioki, H., Namiki, K., Hoshida, T., Kurokawa, H., Ishidate, F., Kaneko, T., Akagi, T.,
1347 Saito, T., Saido, T., et al. (2015). ScaleS: an optical clearing palette for biological imaging. Nat.
1348 Neurosci. *18*, 1518–1529.

1349 Hamnett, R., Dershowitz, L.B., Sampathkumar, V., Wang, Z., Gomez-Frittelli, J., De Andrade,
1350 V., Kasthuri, N., Druckmann, S., Kaltschmidt, J.A. (2022). Regional cytoarchitecture of the adult
1351 and developing mouse enteric nervous system. Curr. Biol. *32*, 1–10.

1352 Hansen, M.B. (2003). The enteric nervous system II: Gastrointestinal functions. Pharmacol.
1353 Toxicol. *92*, 249–257.

1354 He, L., Diedrich, J., Chu, Y.-Y., and Yates, J.R. (2015). Extracting Accurate Precursor
1355 Information for Tandem Mass Spectra by RawConverter. Anal. Chem. *87*, 11361–11367.

1356 Hennig, G.W., Gould, T.W., Koh, S.D., Corrigan, R.D., Heredia, D.J., Shonnard, M.C., and
1357 Smith, T.K. (2015). Use of Genetically Encoded Calcium Indicators (GECIs) Combined with

1358 Advanced Motion Tracking Techniques to Examine the Behavior of Neurons and Glia in the
1359 Enteric Nervous System of the Intact Murine Colon. Front. Cell. Neurosci. *9*, 13819.

1360 Hillmann, B., Al-Ghalith, G.A., Shields-Cutler, R.R., Zhu, Q., Gohl, D.M., Beckman, K.B., Knight,
1361 R., and Knights, D. (2018). Evaluating the Information Content of Shallow Shotgun
1362 Metagenomics. mSystems *3*, 457.

1363 Hofmann, A.F., and Eckmann, L. (2006). How bile acids confer gut mucosal protection against
1364 bacteria. Proceedings of the National Academy of Sciences *103*, 4333–4334.

1365 Huber, W., Heydebreck, von, A., Sültmann, H., Poustka, A., and Vingron, M. (2002). Variance
1366 stabilization applied to microarray data calibration and to the quantification of differential
1367 expression. Bioinformatics *18 Suppl 1*, S96–S104.

1368 Hyland, N.P., and Cryan, J.F. (2010). A Gut Feeling about GABA: Focus on GABA(B)
1369 Receptors. Front Pharmacol *1*, 124.

1370 Ichikawa, R., Takayama, T., Yoneno, K., Kamada, N., Kitazume, M.T., Higuchi, H., Matsuoka,
1371 K., Watanabe, M., Itoh, H., Kanai, T., et al. (2012). Bile acids induce monocyte differentiation
1372 toward interleukin-12 hypo-producing dendritic cells via a TGR5-dependent pathway.
1373 Immunology *136*, 153–162.

1374 Jackson, K.L., Dayton, R.D., Deverman, B.E., and Klein, R.L. (2016). Better Targeting, Better
1375 Efficiency for Wide-Scale Neuronal Transduction with the Synapsin Promoter and AAV-PHP.B.
1376 Front. Mol. Neurosci. *9*, 116.

1377 Jakob, MO., Kofoed-Branzk, M., Deshpande, D., Murugan, S., and Klose, C.S.N. An integrated
1378 view on neuronal subsets in the peripheral nervous system and their role in immunoregulation.
1379 Front. Immunol. *12*, 679055.

1380 Jangi, S., Gandhi, R., Cox, L.M., Li, N., Glehn, von, F., Yan, R., Patel, B., Mazzola, M.A., Liu,
1381 S., Glanz, B.L., et al. (2016). Alterations of the human gut microbiome in multiple sclerosis.
1382 Nature Communications *7*, 12015–11.

1383 Jarret, A., Jackson, R., Duizer, C., Healy, M.E., Zhao, J., Rone, J.M., Bielecki, P., Sefik, E.,
1384 Roulis, M., Rice, T., et al. (2020). Enteric Nervous System-Derived IL-18 Orchestrates Mucosal
1385 Barrier Immunity. Cell *180*, 50–63.e12.

1386 Jia, L., Betters, J.L., and Yu, L. (2011). Niemann-pick C1-like 1 (NPC1L1) protein in intestinal
1387 and hepatic cholesterol transport. Annu. Rev. Physiol. *73*, 239–259.

1388 Johnson, C.D., Barlow-Anacker, A.J., Pierre, J.F., Touw, K., Erickson, C.S., Furness, J.B.,
1389 Epstein, M.L., and Gosain, A. (2018). Deletion of choline acetyltransferase in enteric neurons
1390 results in postnatal intestinal dysmotility and dysbiosis. The FASEB Journal *32*, 4744–4752.

1391 Jones, B.V., Begley, M., Hill, C., Gahan, C.G.M., and Marchesi, J.R. (2008). Functional and
1392 comparative metagenomic analysis of bile salt hydrolase activity in the human gut microbiome.
1393 Proc. Natl. Acad. Sci. U.S.a. *105*, 13580–13585.

1394 Kaelberer, M.M., Buchanan, K.L., Klein, M.E., Barth, B.B., Montoya, M.M., Shen, X., and
1395 Bohórquez, D.V. (2018). A gut-brain neural circuit for nutrient sensory transduction. Science
1396 *361*, eaat5236.

1397 Kaestner, C.L., Smith, E.H., Peirce, S.G., and Hoover, D.B. (2019). Immunohistochemical
1398 analysis of the mouse celiac ganglion: An integrative relay station of the peripheral nervous
1399 system. J. Comp. Neurol. *16*, 2742-2760.

1400 Kim, D., Langmead, B., and Salzberg, S.L. (2015). HISAT: a fast spliced aligner with low
1401 memory requirements. Nat. Methods *12*, 357–360.

1402 Kirwan, W.O., Smith, A.N., Mitchell, W.D., Falconer, J.D., and Eastwood, M.A. (1975). Bile acids
1403 and colonic motility in the rabbit and the human. Gut *16*, 894–902.

1404 Kotterman, M.A., and Schaffer, D.V. (2014). Engineering adeno-associated viruses for clinical
1405 gene therapy. Nat Rev Genet *15*, 445–451.

1406 Kügler, S., Kilic, E., and Bähr, M. (2003). Human synapsin 1 gene promoter confers highly
1407 neuron-specific long-term transgene expression from an adenoviral vector in the adult rat brain
1408 depending on the transduced area. Gene Ther *10*, 337–347.

1409 Lai, N.Y., Musser, M.A., Pinho-Ribeiro, F.A., Baral, P., Jacobson, A., Ma, P., Potts, D.E., Chen,
1410 Z., Paik, D., Soualhi, S., et al. (2019). Gut-Innervating Nociceptor Neurons Regulate Peyer's
1411 Patch Microfold Cells and SFB Levels to Mediate Salmonella Host Defense. Cell *180*, 33–
1412 49.e22.

1413 Langmead, B., and Salzberg, S.L. (2012). Fast gapped-read alignment with Bowtie 2. Nat.
1414 Methods *9*, 357–359.

1415 Latgé, J.P. (2007). The cell wall: a carbohydrate armour for the fungal cell. Molecular
1416 Microbiology *66*, 279–290.

1417 Li, W., and Godzik, A. (2006). Cd-hit: a fast program for clustering and comparing large sets of
1418 protein or nucleotide sequences. Bioinformatics *22*, 1658–1659.

1419 Li, W., Jaroszewski, L., and Godzik, A. (2001). Clustering of highly homologous sequences to
1420 reduce the size of large protein databases. Bioinformatics *17*, 282–283.

1421 Li, W., Yu, G., Liu, Y., and Sha, L. (2019). Intrapancreatic Ganglia and Neural Regulation of
1422 Pancreatic Endocrine Secretion. Front. Neurosci *13,* 21.

1423 Li, Z., Chalazonitis, A., Huang, Y.Y., Mann, J.J., Margolis, K.G., Yang, Q.M., Kim, D.O., Cote,
1424 F., Mallet, J., and Gershon, M.D. (2011). Essential Roles of Enteric Neuronal Serotonin in
1425 Gastrointestinal Motility and the Development/Survival of Enteric Dopaminergic Neurons.
1426 Journal of Neuroscience *31*, 8998–9009.

1427 Lindeberg, J., Usoskin, D., Bengtsson, H., Gustafsson, A., Kylberg, A., Söderström, S., and
1428 Ebendal, T. (2004). Transgenic expression of Cre recombinase from the tyrosine hydroxylase
1429 locus. Genesis *40*, 67–73.

1430 Long, S.L., Gahan, C.G.M., and Joyce, S.A. (2017). Interactions between gut bacteria and bile
1431 in health and disease. Mol. Aspects Med. *56*, 54–65.

1432 Lott, E. L. & Jones, E. B. (2022). Cholinergic Toxicity. StatPearls.

1433 Love, M.I., Huber, W., and Anders, S. (2014). Moderated estimation of fold change and
1434 dispersion for RNA-seq data with DESeq2. Genome Biol *15*, 1–21.

1435 Marotz, C., Amir, A., Humphrey, G., Gaffney, J., Gogul, G., and Knight, R. (2017). DNA
1436 extraction for streamlined metagenomics of diverse environmental samples. Biotechniques. *62*,
1437 290-293.

1438 Martino, C., Morton, J.T., Marotz, C.A., Thompson, L.R., Tripathi, A., Knight, R., and Zengler, K.
1439 (2019). A Novel Sparse Compositional Technique Reveals Microbial Perturbations. mSystems
1440 *4*, 813.

1441 Matheis, F., Muller, P.A., Graves, C.L., Gabanyi, I., Kerner, Z.J., Costa-Borges, D., Ahrends, T.,
1442 Rosenstiel, P., and Mucida, D. (2020). Adrenergic Signaling in Muscularis Macrophages Limits
1443 Infection-Induced Neuronal Loss. Cell *180*, 64–78.e16.

1444 Matsushima, S., Hori, S., and Matsuda, M. (1986). Conversion of 4-aminobutyraldehyde to
1445 gamma-aminobutyric acid in striatum treated with semicarbazide and kainic acid. Neurochem.
1446 Res. *11*, 1313–1319.

1447 McConnell, R.E., Benesh, A.E., Mao, S., Tabb, D.L., and Tyska, M.J. (2011). Proteomic
1448 analysis of the enterocyte brush border. American Journal of Physiology - Gastrointestinal and
1449 Liver Physiology *300*, G914–G926.

1450 McMillin, M., and DeMorrow, S. (2016). Effects of bile acids on neurological function and
1451 disease. Faseb J. *30*, 3658–3668.

1452 McQuade, R. M., Singleton, L. M., Wu, H., Lee, S., Constable, R., Di Natale, M., Ringuet, M. T.,
1453 Berger, J. P., Kauhausen, J., Parish, C. L., Finkelstein, D. I., Furness, J. B., Diwakarla, S.
1454 (2021). The association of enteric neuropathy with gut phenotypes in acute and progressive
1455 models of Parkinson's disease. Scientific Reports *11*.

1456 Mesuere, B., Debyser, G., Aerts, M., Devreese, B., Vandamme, P., and Dawyndt, P. (2015).
1457 The Unipept metaproteomics analysis pipeline. Proteomics *15*, 1437–1442.

1458 Miano, J.M., Miano, J.M., Vlasic, N., Vlasic, N., TOTA, R.R., Tota, R.R., STEMERMAN, M.B.,
1459 and Stemerman, M.B. (1993). Smooth muscle cell immediate-early gene and growth factor
1460 activation follows vascular injury. A putative in vivo mechanism for autocrine growth.
1461 Arterioscler. Thromb. *13*, 211–219.

1462 Mittal, R., Debs, L.H., Patel, A.P., Nguyen, D., Patel, K., O'Connor, G., Grati, M., Mittal, J., Yan,
1463 D., Eshraghi, A.A., et al. (2017). Neurotransmitters: The Critical Modulators Regulating Gut-
1464 Brain Axis. J. Cell. Physiol. *232*, 2359–2372.

1465 Mohanta, S.K., Yin, C., Weber, C., Godinho-Silva, C., Veiga-Fernandes, H., Xu, Q.J., Chang,
1466 R.B., Habenicht, A.J.R. (2023). Cardiovascular Brain Circuits. Circulation Research *11*, 1546-
1467 1565.

1468 Monane, M., Avorn, J., Beers, M.H., Everitt, D.E. (1993). Anticholinergic drug use and bowel
1469 function in nursing home patients. Arch. Intern. Med. *153*, 633-638.

1470 Moran, G.W., Leslie F.C., Levison, S.E., Worthington, J., and McLaughlin, J.T. (2008).
1471 Enteroendocrine cells: neglected players in gastrointestinal disorders? Therap. Adv.
1472 Gastroenterol. *1*, 51-60.

1473 Muller, P.A., Koscsó, B., Rajani, G.M., Stevanovic, K., Berres, M.-L., Hashimoto, D., Mortha, A.,
1474 Leboeuf, M., Li, X.-M., Mucida, D., et al. (2014). Crosstalk between Muscularis Macrophages
1475 and Enteric Neurons Regulates Gastrointestinal Motility. Cell *158*, 1210.

1476 Niesler, B., Kuerten, S., Demir, I.E., and Schäfer, K.H. (2021). Disorders of the enteric nervous
1477 system - a holistic view. Nat Rev Gastroenterol Hepatol. *18*, 393-410.

1478 Nezami, B.G. & Srinivasan, S. (2013). Enteric Nervous System in the Small Intestine:
1479 Pathophysiology and Clinical Implications. Current Gastroenterology Reports *12,* 258-365.

1480 Nishiyama, H., Nagai, T., Kudo, M., Okazaki, Y., Azuma, Y., Watanabe, T., Goto, S., Ogata, H.,
1481 and Sakurai, T. (2018). Supplementation of pancreatic digestive enzymes alters the composition
1482 of intestinal microbiota in mice. Biochem. Biophys. Res. Commun. *495*, 273–279.

1483 Nothias, L.F., Petras, D., Schmid, R., Dührkop, K., Rainer, J., Sarvepalli, A., Protsyuk, I., Ernst,
1484 M., Tsugawa, H., Fleischauer, M., et al. (2019). Feature-based Molecular Networking in the
1485 GNPS Analysis Environment. bioRxiv *38*, 812404.

1486 Olson, C.A., Vuong, H.E., Yano, J.M., Liang, Q.Y., Nusbaum, D.J., and Hsiao, E.Y. (2018). The
1487 Gut Microbiota Mediates the Anti-Seizure Effects of the Ketogenic Diet. Cell *173*, 1728–
1488 1741.e13.

1489 Park, S.K.R., Jung, T., Thuy-Boun, P.S., Wang, A.Y., John R Yates, I., and Wolan, D.W. (2018).
1490 ComPIL 2.0: An Updated Comprehensive Metaproteomics Database. J. Proteome Res. *18*,
1491 616–622.

1492 Park, S.K., Venable, J.D., Xu, T., and Yates, J.R. (2008). A quantitative analysis software tool
1493 for mass spectrometry–based proteomics. Nat. Methods *5*, 319–322.

1494 Peng, J., Elias, J.E., Thoreen, C.C., Licklider, L.J., and Gygi, S.P. (2003). Evaluation of
1495 multidimensional chromatography coupled with tandem mass spectrometry (LC/LC-MS/MS) for
1496 large-scale protein analysis: the yeast proteome. J. Proteome Res. *2*, 43–50.

1497 Pfeiffer, R.F. (2003). Gastrointestinal dysfunction in Parkinson's disease. Lancet Neurol *2*, 107–
1498 116.

1499 Plovier, H., Everard, A., Druart, C., Depommier, C., Van Hul, M., Geurts, L., Chilloux, J.,
1500 Ottman, N., Duparc, T., Lichtenstein, L., et al. (2017). A purified membrane protein from
1501 Akkermansia muciniphila or the pasteurized bacterium improves metabolism in obese and
1502 diabetic mice. Nature Medicine *23*, 107–113.

1503 Pluskal, T., Castillo, S., Villar-Briones, A., and Oresic, M. (2010). MZmine 2: Modular framework
1504 for processing, visualizing, and analyzing mass spectrometry-based molecular profile data.
1505 BMC Bioinformatics *11*.

1506 Qu, Z.D., Thacker, M., Castelucci, P., Bagyánszki, M., Epstein, M.L., Furness, J.B. (2008).
1507 Immunohistochemical analysis of neuron types in the mouse small intestine. Cell and tissue
1508 research *334*, 147–161.

1509 Rajendran, P.S., Challis, R.C., Fowlkes, C.C., Hanna, P., Tompkins, J.D., Jordan, M.C., Hiyari,
1510 S., Gabris-Weber, B.A., Greenbaum, A., Chan, K.Y., et al. (2019). Identification of peripheral
1511 neural circuits that regulate heart rate using optogenetic and viral vector strategies. Nature
1512 Communications 10, 1944.

1513 Rakhilin, N., Barth, B., Choi, J., Muñoz, N.L., Kulkarni, S., Jones, J.S., Small, D.M., Cheng, Y.-
1514 T., Cao, Y., LaVinka, C., et al. (2016). Simultaneous optical and electrical in vivo analysis of the
1515 enteric nervous system. Nature Communications *7*, 31.

1516 Rakhilin, N., Garrett, A., Eom, C.-Y., Chavez, K.R., Small, D.M., Daniel, A.R., Kaelberer, M.M.,
1517 Mejooli, M.A., Huang, Q., Ding, S., et al. (2019). An intravital window to image the colon in real
1518 time. Nature Communications *10*, 5647–10.

1519 Ramirez-Carrozzi, V.R., Braas, D., Bhatt, D.M., Cheng, C.S., Hong, C., Doty, K.R., Black, J.C.,
1520 Hoffmann, A., Carey, M., and Smale, S.T. (2009). A Unifying Model for the Selective Regulation
1521 of Inducible Transcription by CpG Islands and Nucleosome Remodeling. Cell *138*, 114–128.

1522 Rao, M., and Gershon, M.D. (2016). The bowel and beyond: the enteric nervous system in
1523 neurological disorders. Nature Reviews Gastroenterology and Hepatology *13*, 517–528.

1524 Ritchie, M.E., Phipson, B., Wu, D., Hu, Y., Law, C.W., Shi, W., and Smyth, G.K. (2015). limma
1525 powers differential expression analyses for RNA-sequencing and microarray studies. Nucleic
1526 Acids Res *43*, e47–e47.

1527 Rodríguez-Piñeiro, A.M., Bergström, J.H., Ermund, A., Gustafsson, J.K., Schütte, A.,
1528 Johansson, M.E.V., and Hansson, G.C. (2013). Studies of mucus in mouse stomach, small
1529 intestine, and colon. II. Gastrointestinal mucus proteome reveals Muc2 and Muc5ac

1530 accompanied by a set of core proteins. American Journal of Physiology - Gastrointestinal and
1531 Liver Physiology *305*, G348–G356.

1532 Roy, A., Guatimosim, S., Prado, V.F., Gros, R., Prado, M.A. (2015). Cholinergic activity as a
1533 new target in diseases of the heart. Molecular Medicine *20*, 527–537.

1534 Sakai, K., Makino, T., Kawai, Y., and Mutai, M. (1980). Intestinal microflora and bile acids. Effect
1535 of bile acids on the distribution of microflora and bile acid in the digestive tract of the rat.
1536 Microbiol. Immunol. *24*, 187–196.

1537 Samulski, R.J., and Muzyczka, N. (2014). AAV-Mediated Gene Therapy for Research and
1538 Therapeutic Purposes. Annu Rev Virol *1*, 427–451.

1539 Sang, Q., and Young, H.M. (1998). The identification and chemical coding of cholinergic
1540 neurons in the small and large intestine of the mouse. Anat. Rec. *251*, 185–199.

1541 Sannasiddappa, T.H., Lund, P.A., and Clarke, S.R. (2017). In Vitro Antibacterial Activity of
1542 Unconjugated and Conjugated Bile Salts on Staphylococcus aureus. Front. Microbio. *8*, 1581.

1543 Schneider, S., Wright, C.M., and Heuckeroth, R.O. (2019). Unexpected Roles for the Second
1544 Brain: Enteric Nervous System as Master Regulator of Bowel Function. Annu. Rev. Physiol. *81*,
1545 235–259.

1546 Segata, N., Izard, J., Waldron, L., Gevers, D., Miropolsky, L., Garrett, W.S., and Huttenhower,
1547 C. (2011). Metagenomic biomarker discovery and explanation. Genome Biol *12*, R60.

1548 Seillet, C., Luong, K., Tellier, J., Jacquelot, N., Shen, R.D., Hickey, P., Wimmer, V.C.,
1549 Whitehead, L., Rogers, K., Smyth, G.K., et al. (2020). The neuropeptide VIP confers anticipatory
1550 mucosal immunity by regulating ILC3 activity. Nat Immunol *21*, 168–177.

1551 Shan Li, Z., Schmauss, C., Cuenca, A., Ratcliffe, E., Gershon, M. D. (2006). Physiological
1552 Modulation of Intestinal Motility by Enteric Dopaminergic Neurons and the D2 Receptor:
1553 Analysis of Dopamine Receptor Expression, Location, Development, and Function in Wild-Type
1554 and Knock-Out Mice. J Neurosci. *26*, 2798-2807.

1555 Sinha, R., Stanley, G., Gulati, G.S., Ezran, C., Travaglini, K.J., Wei, E., Chan, C.K.F., Nabhan,
1556 A.N., Su, T., Morganti, R.M., et al. (2017). Index switching causes “spreading-of-signal” among
1557 multiplexed samples in Illumina HiSeq 4000 DNA sequencing. *29*, 1072–29.

1558 Steele, P.A., Brookes, S.J., and Costa, M. (1991). Immunohistochemical identification of
1559 cholinergic neurons in the myenteric plexus of guinea-pig small intestine. Neuroscience *45*,
1560 227–239.

1561 Sumner, L.W., Amberg, A., Barrett, D., Beale, M.H., Beger, R., Daykin, C.A., Fan, T.W.M.,
1562 Fiehn, O., Goodacre, R., Griffin, J.L., et al. (2007). Proposed minimum reporting standards for
1563 chemical analysis Chemical Analysis Working Group (CAWG) Metabolomics Standards
1564 Initiative (MSI). Metabolomics *3*, 211–221.

1565 Sundararajan, Z., Knoll, R., Hombach, P., Becker, M., Schultze, J.L., and Ulas, T. (2019). Shiny-
1566 Seq: advanced guided transcriptome analysis. BMC Res Notes *12*, 432–435.

1567 Suzek, B.E., Huang, H., McGarvey, P., Mazumder, R., and Wu, C.H. (2007). UniRef:
1568 comprehensive and non-redundant UniProt reference clusters. Bioinformatics *23*, 1282–1288.

1569 Szklarczyk, D., Gable, A.L., Lyon, D., Junge, A., Wyder, S., Huerta-Cepas, J., Simonovic, M.,
1570 Doncheva, N.T., Morris, J.H., Bork, P., et al. (2019). STRING v11: protein-protein association
1571 networks with increased coverage, supporting functional discovery in genome-wide
1572 experimental datasets. Nucleic Acids Res *47*, D607–D613.

1573 Tabb, D.L., McDonald, W.H., and Yates, J.R. (2002). DTASelect and Contrast: tools for
1574 assembling and comparing protein identifications from shotgun proteomics. J. Proteome Res. *1*,
1575 21–26.

1576 Talbot, J., Hahn, P., Kroehling, L., Nguyen, H., Li, D., and Littman, D.R. (2020). Feeding-
1577 dependent VIP neuron-ILC3 circuit regulates the intestinal barrier. Nature *579*, 575–580.

1578 Tavares-Ferreira, D., Shiers, S., Ray, P.R., Wangzhou, A., Jeevakumar, V., Sankaranarayanan,
1579 I., Cervantes, A.M., Reese, J.C., Chamessian, A., Copits, B.A., Dougherty, P.M., Gereau, R.W.,
1580 Burton, M.D., Dussor, G., and Price, T.J. (2022). Spatial transcriptomics of the dorsal root
1581 ganglia identifies molecular signatures of human nociceptors. Sci. Transl. Med. *14*, eabj8186.

1582 Thompson, K.J., Khajehali, E., Bradley, S.J., Navarrete, J.S., Huang, X.P., Slocum, S., Jin, J.,
1583 Liu, J., Xiong, Y., Olsen, R.H.J., et al. (2018). DREADD Agonist 21 Is an Effective Agonist for
1584 Muscarinic-Based DREADDs in Vitro and in Vivo. ACS Pharmacol Transl Sci *1*, 61–72.

1585 Treweek, J.B., Chan, K.Y., Flytzanis, N.C., Yang, B., Deverman, B.E., Greenbaum, A., Lignell,
1586 A., Xiao, C., Cai, L., Ladinsky, M.S., et al. (2015). Whole-body tissue stabilization and selective
1587 extractions via tissue-hydrogel hybrids for high-resolution intact circuit mapping and
1588 phenotyping. Nature Protocols *10*, 1860–1896.

1589 Truong, D.T., Franzosa, E.A., Tickle, T.L., Scholz, M., Weingart, G., Pasolli, E., Tett, A.,
1590 Huttenhower, C., and Segata, N. (2015). MetaPhlAn2 for enhanced metagenomic taxonomic
1591 profiling. Nat. Methods *12*, 902–903.

1592 Valicenti-McDermott, M.D., McVicar, K., Cohen, H.J., Wershil, B.K., and Shinnar, S. (2008).
1593 Gastrointestinal symptoms in children with an autism spectrum disorder and language
1594 regression. Pediatr. Neurol. *39*, 392–398.

1595 Van Herreweghen, F., Van den Abbeele, P., De Mulder, T., De Weirdt, R., Geirnaert, A.,
1596 Hernandez-Sanabria, E., Vilchez-Vargas, R., Jauregui, R., Pieper, D.H., Belzer, C., et al.
1597 (2017). In vitro colonisation of the distal colon by Akkermansia muciniphila is largely mucin and
1598 pH dependent. Benef Microbes *8*, 81–96.

1599 Vavassori, P., Mencarelli, A., Renga, B., Distrutti, E., and Fiorucci, S. (2009). The bile acid
1600 receptor FXR is a modulator of intestinal innate immunity. J Immunol *183*, 6251–6261.

1601 Walsh, K.T., and Zemper, A.E. (2019). The Enteric Nervous System for Epithelial Researchers:
1602 Basic Anatomy, Techniques, and Interactions With the Epithelium. Cellular and Molecular
1603 Gastroenterology and Hepatology *8*, 369–378.

1604 Wang, H. Foong, J. P. P., Harris, N. L., Bornstein, J. C. (2022). Enteric neuroimmune
1605 interactions coordinate intestinal responses in health and disease. Mucosal Immunology 15, 27-
1606 39.

1607 Wang, M., Carver, J.J., Phelan, V.V., Sanchez, L.M., Garg, N., Peng, Y., Nguyen, D.D.,
1608 Watrous, J., Kapono, C.A., Luzzatto-Knaan, T., et al. (2016). Sharing and community curation of
1609 mass spectrometry data with Global Natural Products Social Molecular Networking. Nat
1610 Biotechnol *34*, 828–837.

1611 Watanabe, M., Houten, S.M., Mataki, C., Christoffolete, M.A., Kim, B.W., Sato, H., Messaddeq,
1612 N., Harney, J.W., Ezaki, O., Kodama, T., et al. (2006). Bile acids induce energy expenditure by
1613 promoting intracellular thyroid hormone activation. Nature *439*, 484–489.

1614 Wess, J., Nakajima, K., and Jain, S. (2013). Novel designer receptors to probe GPCR signaling
1615 and physiology. Trends Pharmacol. Sci. *34*, 385–392.

1616 Wessel, D., and Flügge, U.I. (1984). A method for the quantitative recovery of protein in dilute
1617 solution in the presence of detergents and lipids. Analytical Biochemistry *138*, 141–143.

1618 Whitcomb, D.C., and Lowe, M.E. (2007). Human pancreatic digestive enzymes. Dig. Dis. Sci.
1619 *52*, 1–17.

1620 Wu, Y.E., Pan, L., Zuo, Y., Li, X., and Hong, W. (2017). Detecting Activated Cell Populations
1621 Using Single-Cell RNA-Seq. Neuron *96*, 313–329.e316.

1622 Xu, T., Park, S.K., Venable, J.D., Wohlschlegel, J.A., Diedrich, J.K., Cociorva, D., Lu, B., Liao,
1623 L., Hewel, J., Han, X., et al. (2015). ProLuCID: An improved SEQUEST-like algorithm with
1624 enhanced sensitivity and specificity. J Proteomics *129*, 16–24.

1625 Xu, T., Venable, J.D., Park, S.K., Cociorva, D., Lu, Q.B., Liao, L., Wohlschlegel, J., Hewel, J.,
1626 Yates, J.R., and Conciorva, D. (2006). ProLuCID, a fast and sensitive tandem mass spectra-
1627 based protein identification program.

1628 Yang, B., Treweek, J.B., Kulkarni, R.P., Deverman, B.E., Chen, C.-K., Lubeck, E., Shah, S.,
1629 Cai, L., and Gradinaru, V. (2014). Single-Cell Phenotyping within Transparent Intact Tissue
1630 through Whole-Body Clearing. Cell *158*, 945–958.

1631 Yano, J.M., Yu, K., Donaldson, G.P., Shastri, G.G., Ann, P., Ma, L., Nagler, C.R., Ismagilov,
1632 R.F., Mazmanian, S.K., and Hsiao, E.Y. (2015). Indigenous Bacteria from the Gut Microbiota
1633 Regulate Host Serotonin Biosynthesis. Cell *161*, 264–276.

1634 Zhang, H., Sparks, J.B., Karyala, S.V., Settlage, R., and Luo, X.M. (2015). Host adaptive
1635 immunity alters gut microbiota. Isme J *9*, 770–781.

1636 Zhang, X., Smits, A.H., van Tilburg, G.B., Ovaa, H., Huber, W., and Vermeulen, M. (2018).
1637 Proteome-wide identification of ubiquitin interactions using UbIA-MS. Nature Protocols *13*, 530–
1638 550.

1639 Zhu, Q., Mai, U., Pfeiffer, W., Janssen, S., Asnicar, F., Sanders, J.G., Belda-Ferre, P., Al-
1640 Ghalith, G.A., Kopylova, E., McDonald, D., et al. (2019). Phylogenomics of 10,575 genomes
1641 reveals evolutionary proximity between domains Bacteria and Archaea. Nature Communications
1642 *10*, 5477–14.